



Chinese Pharmaceutical Association
Institute of Materia Medica, Chinese Academy of Medical Sciences

Acta Pharmaceutica Sinica B

www.elsevier.com/locate/apsb
www.sciencedirect.com



ORIGINAL ARTICLE

PIM1–HDAC2 axis modulates intestinal homeostasis through epigenetic modification



Jianming Yang^{a,†}, Yawen Xiao^{a,†}, Ningning Zhao^a, Geng Pei^b, Yan Sun^b, Xinyu Sun^a, Kaiyuan Yu^a, Chunhui Miao^a, Ran Liu^a, Junqiang Lv^a, Hongyu Chu^c, Lu Zhou^c, Bangmao Wang^c, Zhi Yao^{a,*}, Quan Wang^{a,*}

^aKey Laboratory of Immune Microenvironment and Disease (Ministry of Education), Tianjin Institute of Immunology, State Key Laboratory of Experimental Hematology, the Province and Ministry Co-sponsored Collaborative Innovation Center for Medical Epigenetics, Department of Immunology, School of Basic Medical Sciences, Tianjin Institute of Urology, the Second Hospital of Tianjin Medical University, Tianjin Key Laboratory of Cellular and Molecular Immunology, Tianjin Medical University, Tianjin 300070, China

^bDepartment of Pathology, Tianjin Medical University Cancer Institute and Hospital; National Clinical Research Center of Cancer; Key Laboratory of Cancer Prevention and Therapy, Tianjin; Tianjin's Clinical Research Center of Cancer, Tianjin 30060, China

^cDepartment of Gastroenterology and Hepatology, Tianjin Medical University General Hospital, Tianjin Medical University, Tianjin 300070, China

Received 11 October 2023; received in revised form 7 March 2024; accepted 14 March 2024

KEY WORDS

PIM1;
HDAC2;
Goblet cell;
Gut microbiota;
Intestinal homeostasis;
Epigenetic modification;
Ulcerative colitis;
CAC

Abstract The mucosal barrier is crucial for intestinal homeostasis, and goblet cells are essential for maintaining the mucosal barrier integrity. The proviral integration site for Moloney murine leukemia virus-1 (PIM1) kinase regulates multiple cellular functions, but its role in intestinal homeostasis during colitis is unknown. Here, we demonstrate that PIM1 is prominently elevated in the colonic epithelia of both ulcerative colitis patients and murine models, in the presence of intestinal microbiota. Epithelial PIM1 leads to decreased goblet cells, thus impairing resistance to colitis and colitis-associated colorectal cancer (CAC) in mice. Mechanistically, PIM1 modulates goblet cell differentiation through the Wnt and Notch signaling pathways. Interestingly, PIM1 interacts with histone deacetylase 2 (HDAC2) and down-regulates its level *via* phosphorylation, thereby altering the epigenetic profiles of Wnt signaling pathway

*Corresponding authors.

E-mail addresses: wangquan@tmu.edu.cn (Quan Wang), yaozhi@tmu.edu.cn (Zhi Yao).

†These authors made equal contributions to this work.

Peer review under the responsibility of Chinese Pharmaceutical Association and Institute of Materia Medica, Chinese Academy of Medical Sciences.

<https://doi.org/10.1016/j.apsb.2024.04.017>

2211-3835 © 2024 The Authors. Published by Elsevier B.V. on behalf of Chinese Pharmaceutical Association and Institute of Materia Medica, Chinese Academy of Medical Sciences. This is an open access article under the CC BY-NC-ND license (<http://creativecommons.org/licenses/by-nc-nd/4.0/>).

genes. Collectively, these findings investigate the unknown function of the PIM1–HDAC2 axis in goblet cell differentiation and ulcerative colitis/CAC pathogenesis, which points to the potential for PIM1-targeted therapies of ulcerative colitis and CAC.

© 2024 The Authors. Published by Elsevier B.V. on behalf of Chinese Pharmaceutical Association and Institute of Materia Medica, Chinese Academy of Medical Sciences. This is an open access article under the CC BY-NC-ND license (<http://creativecommons.org/licenses/by-nc-nd/4.0/>).

1. Introduction

Ulcerative colitis (UC) is a chronic inflammatory bowel disease characterized by mucosal inflammation and ulceration in the colon and rectum¹. It affects millions of people worldwide and significantly burdens global health care². The exact etiology of UC remains elusive, but it is thought to arise from the complex interplay of genetic factors, environmental factors, epithelial barrier defects, and dysregulated immune responses³. Among these factors, the intestinal mucosal barrier function is essential for maintaining immune homeostasis as it ensures the complex crosstalk between the gut microbiota and the host immune system^{4,5}. Therefore, maintaining the intestinal mucosal barrier integrity and functions has been recognized as a critical player in gut homeostasis maintenance⁶.

Among the various components of the mucosal barrier, colonic goblet cells serve a crucial role in maintaining mucosal integrity⁷. Goblet cells are specialized epithelial cells that synthesize and secrete mucins, the major structural components of mucus. Mucus layers covering the intestinal epithelial cells provide a protective barrier that prevents pathogenic microbial invasion and colonization⁸. Several studies have revealed that altered goblet cell numbers, reduced mucin production, and disrupted mucus layers contribute to the occurrence and progression of UC^{9–11}. The Notch and Wnt signaling pathways are crucial for goblet cell differentiation^{7,12,13}.

The proviral integration site for Moloney murine leukemia virus-1 (*PIMI*) is a proto-oncogene encoding a serine/threonine kinase¹⁴. PIM1 kinase is constitutively active and involved in various cellular processes, including cell survival, proliferation, and differentiation, by phosphorylating a wide range of substrates^{15,16}. PIM1 kinase has been linked to several malignancies^{17,18}. Some studies have explored the role of PIM1 kinase in animal models of autoimmune diseases, such as experimental autoimmune uveitis (EAU) and systemic lupus erythematosus (SLE)^{19,20}. Emerging evidence suggests that the PIM1 inhibitor attenuates trinitrobenzene sulphonic acid (TNBS) and dextran sodium sulfate (DSS)-induced colitis in mice^{21,22}. However, its role in UC and the underlying mechanisms remain unknown.

HDAC2, a class I histone deacetylase, removes acetyl groups from lysine residues in histones to suppress gene transcription. HDAC2 primarily targets histones H3 and H4 and some non-histone substrates. HDAC2 is predominantly located in the nucleus and undergoes various posttranslational modifications, including acetylations, phosphorylations, nitrosylations, and sumoylations²³. It has been reported to play essential roles in cellular proliferation, cell migration, cell senescence, cell apoptosis, inflammation, and gene expression regulation, which contribute to the pathogenesis of various diseases^{24,25}. Evidence suggests that HDAC overexpression is a biomarker for tumorigenesis, such as HDAC1/2/3, which is upregulated in human

cervical cancer cells and tissues^{26,27}. Inhibitors that target abnormal HDACs have shown promising antitumor effects. Recent studies have also implicated HDAC2 as essential for IEC homeostasis and inflammatory responses²⁸. Nevertheless, the function and underlying mechanisms of HDAC2 in UC have not yet been determined.

In this study, we report the role of PIM1 in UC and its impact on colonic goblet cell differentiation, which is critical for maintaining mucosal homeostasis. Mechanistically, PIM1 modulates goblet cell differentiation by regulating Wnt and Notch signaling pathways, partially mediated by its binding, phosphorylating, and downregulating of HDAC2. Our findings emphasize the complex interplay between PIM1–HDAC2 and UC pathogenesis and highlight the potential of PIM1 and HDAC2 as diagnostic indicators and therapeutic targets.

2. Materials and methods

2.1. Mice

All mice used in this study were on the C57BL/6J background. *Pim1* heterozygous (*Pim1*^{+/-}) and *Pim1* homozygous (*Pim1*^{-/-}) were generated from Biocytogen Pharmaceuticals (Beijing, China) and were confirmed by PCR genotype analysis. *Pim1*^{KI} and Villin-Cre mice were purchased from GemPharmatech (Nanjing, China). Wild-type male C57BL/6J mice were obtained from the Academy of Military Medical Science (Beijing, China). Mice were housed in a specific pathogen-free environment at the Department of Laboratory Animal Science and Technology of Tianjin Medical University. Unless otherwise specified, they were used for experiments at 6–8 weeks of age. All animal experiments were approved by the Animal Care and Use Committee of Tianjin Medical University (TMUamec 2021039).

2.2. Human samples

Colonic tissue samples were collected from patients diagnosed with ulcerative colitis at Tianjin Medical University General Hospital. Colonic tissue samples were collected from patients diagnosed with colorectal cancer (CRC) at Tianjin Medical University Cancer Institute and Hospital. The diagnosis was made based on colonoscopy and pathological examination of the collected tissue. Relevant clinical information for the patients is presented in [Supporting Information Table S1](#). The human CRC tissue chip was obtained from Guilin Fanpu Biotechnology Co., Ltd. (Guilin, China). All samples were obtained with the informed consent of the patients ([Supporting Information Fig. S1](#)), and the study was approved by the Ethics Committee of Tianjin Medical University General Hospital (IRB2020-KY-190) or the Ethics Committee of Tianjin Medical University Cancer Institute and

Hospital (bc2023182) or Guilin Fanpu Biotechnology Co., Ltd. (Fanpu [2018] No. 23).

2.3. Cell lines and reagents

The human colon adenocarcinoma cell lines Caco2 (ATCC HTB-37) and human embryonic kidney 293T cell (ATCC CRL-3216) were obtained from ATCC. Caco2 cells were maintained in RPMI 1640 medium supplemented with 20% fetal bovine serum. 293T cells were cultured in Dulbecco's modified Eagle's medium (DMEM) supplemented with 10% fetal bovine serum. Cells were incubated at 37 °C in a humidified incubator containing 5% CO₂. The Wnt activator (10 μmol/L; 252917-06-9, MedChemExpress, NJ, USA) and Notch inhibitor (5 μmol/L; 208255-80-5, MedChemExpress) were dissolved in DMSO (D8372, Solarbio, Beijing, China) and added to the culture medium for 24 h.

2.4. GEO datasets

We employed six datasets to analyze *PIM1* gene expression. The microarray data obtained from the Gene Expression Omnibus (GSE75214, GSE65114, GSE47908, GSE37364, GSE44861, and GSE4183) were processed using Sanger Box software.

2.5. ScRNA-seq analysis

The *PIM1* expression was analyzed by Majorbio Bio-Pharm Technology Co., Ltd. (Shanghai, China) in the colon biopsies of patients with UC using Single-cell RNA sequencing (scRNA-seq) data on the Broad Institute Single Cell portal (https://singlecell.broadinstitute.org/single_cell/study/SCP259/intra-and-inter-cellular-rewiring-of-the-human-colon-during-ulcerative-colitis).

2.6. DSS-induced acute colitis mouse model

For the DSS-induced acute colitis mouse model, mice were administered 1.5% DSS (0216011090, MV = 36–50 kDa, MP Biomedicals, OH, USA) dissolved in drinking water for seven days. Weight, rectal bleeding, and stool consistency were assessed daily and scored according to previously described methods²⁹. The disease activity index (DAI) was evaluated based on body weight loss, rectal bleeding, and stool consistency. Body weight loss was categorized as follows: 0 (<2%), 1 (2%–5%), 2 (5%–10%), 3 (10%–15%), and 4 (≥15%). Rectal bleeding was categorized as follows: 0, normal; 1, brown color; 2, reddish color; 3, bloody stool. Stool consistency was organized as follows: 0, normal; 1, mild soft stools; 2, very soft stools; 3, watery stools. On the seventh day, the mice were euthanized, and colon tissues were harvested. The distal part of the colon was fixed in 4% paraformaldehyde and embedded in paraffin for subsequent histological analysis. Another portion of the distal colon was embedded in an optimal cutting temperature (OCT, 4583, Sakura Finetek, USA) compound, rapidly frozen in liquid nitrogen, and stored at –80 °C until further use.

2.7. Intestinal permeability

After mice were administered 1.5% DSS in drinking water for six days, they were gavaged orally with FITC-dextran (0.6 mg/g body weight, Sigma–Aldrich, Germany). After 4 h, the blood was collected by cardiac puncture. Subsequently, blood serum was analyzed for measuring fluorescence intensity with Synergy HT

Multi-Mode Microplate Reader (Bio-tek Winooski, VT, USA) at an excitation wavelength of 485 nm and emission wavelength of 525 nm.

2.8. Hematoxylin and eosin (H&E) staining

The distal colon tissue was fixed with 4% paraformaldehyde to perform histological analysis and then embedded in paraffin. The tissue was sectioned into 5 μm slices and stained with hematoxylin and eosin. Images were captured using a microscope (BX46, Olympus, Tokyo, Japan). The histological score was assessed based on previously established criteria²⁹. Briefly, the histological score was scored with seven parameters: degree of inflammation (0–4), the severity of crypt damage (0–4), immune cell infiltration (0–3), submucosal edema (0–3), loss of goblet cells (0–3), active epithelial hyperplasia (0–3), and crypt abscesses (0–2).

We used the AB-PAS Stain Kit (Solarbio, Beijing, China) according to the manufacturer's guidelines to detect goblet cells. Goblet cell quantification was performed by counting the total number of goblet cells within crypts from four fields.

2.9. Immunohistochemistry

Paraffin-embedded colon tissue sections were deparaffinized using xylene and dehydrated using alcohol, then subjected to antigen retrieval in citrate buffer (pH 6.0). The sections were treated with 0.3% hydrogen peroxide to block endogenous peroxidase activity and blocked with 5% normal goat serum for 1 h. The sections were incubated overnight with primary antibodies against MUC2 (1:1000, Proteintech, Chicago, IL, USA), HDAC2 (1:1000, Proteintech), LGR5 (1:400, Affinity Biosciences, Cincinnati, OH, USA), cleaved caspase-3 (1:2000, Cell Signaling Technology, Danvers, MA, USA), ZO-1 (1:500, Thermofisher Scientific, Waltham, MA, USA), PIM1 (1:200, Thermofisher Scientific, USA), and OCCLUDIN (1:200, Abcam, Cambridge, MA, USA). After washing with PBS at least five times, the sections were incubated with horseradish peroxidase (HRP)-labeled secondary antibody (Zsbio, Beijing, China) for 30 min. Diaminobenzidine chromogenic substrate (Zsbio) was used to develop the staining. Hematoxylin was applied as a counterstain, and the sections were dehydrated and mounted. Tissue samples were imaged using an Olympus BX46 microscope (OLYMPUS, Japan). Staining intensity was quantified using the Image Pro Plus software.

2.10. Immunofluorescent staining

5 μm sections were cut from tissues embedded in OCT compounds. The sections were treated with cold acetone for 10 min at 4 °C to fix. Tissues were blocked using 5% BSA for 1 h, followed by incubation overnight with the indicated primary antibody against MUC2 (1:500, Proteintech). The samples were washed with PBS and then incubated with Alexa Fluor 488-labeled second antibody (1:500, Proteintech) for 1 h. After washing thoroughly, the sections were mounted with DAPI Fluoromount-G gum and imaged using a confocal fluorescence microscope (Leica TCS-SP8, Leica Microsystems, Germany).

Cells were fixed with 4% paraformaldehyde for 15 min and then permeabilized with 0.25% TritonX-100 for 10 min. The cells were treated with 5% normal goat serum for 1 h to block non-specific binding before being incubated with primary antibodies against MUC2 (1:500, Proteintech), FLAG (1:1000, Sigma–Aldrich), and HDAC2 (1:1000, Proteintech) overnight. After

washing, the samples were incubated with Alexa Fluor 488- or Alexa Fluor 594-labeled second antibody (1:500, Proteintech). Subsequently, fluorescence imaging was carried out using a fluorescence microscope (OLYMPUS IX73, OLYMPUS, Japan).

2.11. Fecal microbiota transplantation

200 mg of stool was collected daily from WT donor mice or DSS-induced colitis donor mice. The stool was resuspended in 1 mL sterile anaerobic PBS and then passed through a 70- μ m filter. WT recipient mice were pretreated with a cocktail of broad-spectrum antibiotics for seven days and then were intragastrically administered with 0.2 mL fresh fecal solution of WT donor mice or DSS-induced colitis donor mice once daily for seven days.

2.12. Proximity ligation assay

Proximity ligation assay was performed using Duolink In Situ Proximity Ligation Assay kit (DUO92013, Sigma–Aldrich) according to the manufacturer's instructions. Cells were fixed with 4% paraformaldehyde for 10 min at room temperature, followed by permeabilization with 0.25% TritonX-100 for 15 min at room temperature. The cells were blocked using 1 \times blocking solution for 60 min at 37 °C to block non-specific binding. Cells were then incubated with primary antibodies against FLAG (1:1000, Sigma–Aldrich) and HDAC2 (1:500, Abcam) overnight at 4 °C. After washing with wash buffer A, cells were incubated with PLA probes at 37 °C for 60 min. Subsequently, the cells were rewashed in wash buffer A and incubated in ligation solution for 30 min at 37 °C. Afterward, cells were washed two times with wash buffer A and incubated with an amplification solution at 37 °C for 100 min. Finally, the cells were washed two times with wash buffer B and mounted with DAPI Fluoromount-G gum. Fluorescence imaging was carried out using a confocal fluorescence microscope (Leica TCS-SP8, Leica Microsystems).

2.13. RNA extraction and real-time PCR

Total RNA from colon tissue and Caco2 cells were extracted using the TRizol reagent (Solarbio, Beijing, China) following the manufacturer's instructions. MonScript™ RTIII All-in-One Mix (Monad, Suzhou, China) was used to reverse-transcribe 1 μ g of total RNA to cDNA. Quantitative real-time PCR was performed in triplicate using SYBR Green qPCR Master mixes (Cwbio, Jiangsu, China) under the thermocycler PCR system (LightCycler 96, Roche). The relative gene expression was calculated using the $2^{-\Delta\Delta CT}$ method. β -Actin was used as an internal control. The primer sequences are listed in [Supporting Information Table S2](#).

2.14. Isolation of mesenteric lymph nodes (MLN) and colonic lamina propria cells

We obtained lymphocytes from the mesenteric lymph nodes (MLN). The nodes were directly ground using a 70- μ m cell strainer with RPMI 1640 medium supplemented with 10% FBS. The resulting mixture was centrifuged, and the cells were then suspended in RPMI 1640 medium for further evaluation.

To obtain lymphocytes from the colonic lamina propria, the colon tissues were first cut into 1 cm pieces in cold PBS. These pieces were then incubated with cold PBS containing 2 mmol/L dithiothreitol (DTT) at 150 rpm (Eppendorf Centrifuge 5424R, Hamburg, Germany) and 37 °C for 10 min, followed by

incubation with cold PBS containing 5 mmol/L EDTA three times at 150 rpm (Eppendorf Centrifuge 5424R) and 37 °C for 10 min each. Next, the colon tissue was minced using scissors and digested in 1 mL of a solution containing 0.5 mg/mL collagenase (Sigma–Aldrich), 0.05 mg/mL hyaluronic acid, 100 ng/mL DNase I in RPMI 1640 medium at 150 rpm (Eppendorf Centrifuge 5424R) and 37 °C for 30 min. After digestion, the cell solution was filtered through a 70- μ m cell strainer and suspended in 40% Percoll (Healthcare, Chicago, IL, USA). The suspension was centrifuged at 670 \times g (Eppendorf Centrifuge 5810R, Hamburg, Germany) for 30 min at 4 °C.

2.15. Flow cytometry

For cell surface staining, single-cell suspensions were stained with the following antibodies for 30 min at 4 °C in the dark: anti-CD45 conjugated to APC (1:100, 103111, Biolegend, San Diego, CA, USA), anti-CD11b conjugated to PE-Cy7 (1:100, 25-0112-81, Invitrogen, Waltham, MA, USA), anti-F4/80 conjugated to FITC (1:100, 11-4801-85, eBioscience, San Diego, CA, USA), anti-CD45 conjugated to APC-Cy7 (1:100, 103116, Biolegend), anti-MHCII conjugated to PE (1:100, 107607, Biolegend), anti-CD11c conjugated to APC (1:100, 117309, Biolegend), anti-CD45 conjugated to PerCP/Cy5.5 (1:100, 103132, Biolegend), anti-Ly6G conjugated to APC (1:100, 127614, Biolegend).

For intracellular cytokine staining, single-cell suspensions were stimulated with cell activation cocktail containing Brefeldin A for 5 h at 37 °C. After the stimulation, cells were washed with PBS and stained with Zombie NIRT™ Fixable Viability Kit (1:1000, 423105, Biolegend) for 30 min at 4 °C and then incubated with the following antibodies: anti-CD3 conjugated to FITC (1:100, 100204, Biolegend), anti-CD4 conjugated to PE-Cy7 (1:100, 100422, Biolegend). Subsequently, the cells were fixed using a fixation buffer (420801, Biolegend) and permeabilized with an intracellular staining permeabilization wash buffer (421002, Biolegend) according to the manufacturer's instructions. Cells were then incubated for 30 min at 4 °C with the following antibodies: anti-IL-17A conjugated to APC (1:100, 509616, Biolegend), anti-IFN- γ conjugated to PerCP/Cy5.5 (1:100, 45-7311-82, Invitrogen), anti-IL-4 conjugated to PE (1:100, 504103, Biolegend). The cells were subjected to staining using the following antibodies: anti-CD3 labeled with FITC (1:100, 100204, Biolegend), anti-CD4 labeled with PE-Cy7 (1:100, 100422, Biolegend), and anti-CD25 labeled with PE (1:100, 102008, Biolegend) to analyze Treg cells. Subsequently, the cells were fixed and permeabilized using the Foxp3/transcription factor staining buffer sets (00-5523-00, eBioscience, Waltham, MA, USA) according to the manufacturer's instructions. This was followed by staining with anti-Foxp3 labeled with APC (1:100, 320014, Biolegend). The acquired data were analyzed using the FlowJo software (FlowJo, Ashland, OR, USA) on the FACS Canto II Flow Cytometer (BD Biosciences).

2.16. Western blotting

The distal colon was homogenized in RIPA lysis buffer supplemented with complete protease inhibitors (Roche, Mannheim, Germany). Protein lysates were boiled with 5 \times SDS buffer at 99 °C for 10 min. Samples were then separated by 10% SDS-PAGE gels and transferred to the PVDF membrane. After blocking with 5% milk for 1 h, the PVDF membrane was incubated with primary antibodies anti-PIM1 antibody (1:1000, Thermofisher

Scientific, USA) overnight in 4 °C. Subsequently, and the membrane was incubated with the corresponding HRP-conjugated secondary antibodies for 1 h. Signals were detected with Immobilon Western Chemiluminescent HRP Substrate (Merck Millipore, Billerica, MA, USA).

Cells were lysed in an ice-cold lysis buffer supplemented with complete protease inhibitors. The cell lysates were collected and boiled at 99 °C for 10 min, then loaded onto 10% SDS-PAGE gels. After electrophoresis, proteins were transferred to PVDF membranes and blocked with 5% milk for 1 h. The membranes were further probed with the indicated primary antibodies overnight at 4 °C. The following primary antibodies were used: anti-PIM1 antibody (1:1000, Thermofisher Scientific, USA), anti-HDAC2 antibody (1:1000, Abcam), anti-FLAG antibody (1:1000, Sigma-Aldrich, USA), anti-MYC antibody (1:1000, Cell Signaling Technology, USA). The next day, the membrane was incubated with the corresponding HRP-conjugated secondary antibodies for 1 h. The protein bands were detected with Immobilon Western Chemiluminescent HRP Substrate (Merck Millipore, Billerica, MA, USA). Densitometry was performed using ImageJ software (National Institutes of Health, Bethesda, USA).

2.17. Antibiotic treatment

Mice received the antibiotic cocktail (Abx, ampicillin (1 g/L), neomycin (1 g/L), metronidazole (1 g/L), and vancomycin (500 mg/L), SangonBiotech, Shanghai, China) with drinking water for seven days to clear gut microbiota. Abx-containing water was replaced every 3–4 days. Mice were administered 1.5% DSS in drinking water for seven days, after which colon tissues were collected on the 7th.

2.18. Co-housing experiment

For the co-housing experiments, two male WT and two male *Pim1*^{+/-} mice (4 weeks of age) were co-housed in a single cage for 4 weeks. At least three cages were used to co-house WT and *Pim1*^{+/-}. After co-housing, the mice were subjected to 1.5% DSS treatment for 7 days. Colon tissues and fecal samples were collected.

2.19. IECs harvest

The colons from WT and *Pim1*^{+/-} mice were cut longitudinally and then divided into 1 cm pieces to incubate in ice-cold PBS containing 30 mmol/L EDTA and 1.5 mmol/L DTT for 30 min. The remaining colons were then suspended in PBS containing 30 mmol/L EDTA at 37 °C for 10 min. Samples were shaken gently for 30 s to release epithelium from the basement membrane. After removing the remnant intestinal tissue, IECs were centrifuged at 1000 rpm (Eppendorf Centrifuge 5424R) for 5 min at 4 °C. The IECs were washed with ice-cold PBS at 4 °C and then were lysed in Trizol reagent (Invitrogen) for RNA extraction or lysed in lysis buffer for immunoprecipitation assays.

2.20. Silver staining and mass spectrometry

Cellular extracts of Caco2 cells transfected with vector or FLAG-PIM1 were incubated with anti-FLAG beads overnight at 4 °C with constant rotation. After centrifugation, the beads were thoroughly washed, treated with SDS loading buffer, and analyzed by SDS-PAGE and silver stained. Silver staining was performed

using the Pierce silver stain kit (24612, Thermofisher Scientific) following the manufacturer's instructions and then subjected to LC-MS/MS analysis.

2.21. Immunoprecipitation (IP) assays

The harvested IECs and Caco2 cells were washed with pre-chilled PBS and lysed in a lysis buffer containing complete mini-EDTA-free protease inhibitor cocktail tablets (Roche) on ice for 30 min. Cell supernatants were collected at 12,000×g (Eppendorf Centrifuge 5424R) for 30 min to remove cell debris. For immunoprecipitation of FLAG-tagged or MYC-tagged proteins, cell lysates were incubated with either anti-FLAG beads or anti-MYC beads overnight at 4 °C with constant rotation, followed by centrifugation at 500×g (Eppendorf Centrifuge 5424R) and washed with binding buffer (2 mmol/L EDTA, 50 mmol/L Tris-HCl (pH 7.4), 150 mmol/L NaCl, 0.1% NP-40, 30% glycerol). Then, the beads were thoroughly washed, treated with SDS loading buffer, and analyzed by SDS-PAGE and Western blotting.

For immunoprecipitation of endogenous proteins, IECs and Caco2 cell lysates were incubated with anti-HDAC2 antibody or immunoglobulin G (IgG, 3420S, Cell Signaling Technology) overnight at 4 °C with constant rotation and subsequently incubated with Protein A/G beads (20241, Thermofisher Scientific) for 2 h. After incubation, the beads were thoroughly washed, treated with SDS loading buffer, and analyzed by SDS-PAGE and Western blotting.

2.22. 16S rRNA-sequencing

According to the manufacturer's recommendations, fecal genomic DNA was extracted from each mouse using the Stool DNA Kit (D4015-02, Omega Bio-tek, Norcross, GA, USA). The final DNA concentration and purity were determined using a NanoDrop 2000 UV-Vis spectrophotometer (Nanodrop Technologies, Wilmington, DE, USA).

16S rRNA gene sequencing was performed by Majorbio Bio-Pharm Technology Co., Ltd. (Shanghai, China). The 16S libraries were amplified by 515F/806R primer targeting the 16S rRNA gene hypervariable V3 and V4 regions. The purified products were quantified using a QuantiFluor™-ST (Promega, Madison, WI, USA) according to the manufacturer's protocol. The purified amplicons were pooled in equimolar amounts and paired-end sequenced (2 × 300 bp) on an Illumina MiSeq platform (Illumina, San Diego, CA, USA) according to the standard protocols by Majorbio Bio-Pharm Technology Co., Ltd. (Shanghai, China). The raw reads were deposited in the NCBI Sequence Read Archive (SRA) database (Accession No.: SRP440557).

2.23. RNA sequencing

Total RNA from IECs and Caco2 cells were extracted using TRIzol Reagent, following the manufacturer's instructions (Invitrogen). The quality of the extracted RNA was assessed using a 2100 Bioanalyzer (Agilent, CA, USA), and the RNA concentration was determined using the ND-2000 (NanoDrop Technologies). For RNA sequencing (RNA-seq), a transcriptome library was prepared using the TruSeq™ RNA sample preparation Kit from Illumina (San Diego, CA, USA). Paired-end RNAseq sequencing libraries were sequenced on the Illumina NovaSeq 6000 sequencer with 2 × 150 bp read length, following standard

protocols provided by Majorbio Bio-Pharm Technology Co., Ltd. or LC-Bio Technology Co., Ltd.

The raw paired-end reads obtained were subjected to trimming and quality control using SeqPrep (<https://github.com/jstjohn/SeqPrep>) and Sickle (<https://github.com/najoshi/sickle>) with default parameters. Subsequently, the clean reads were aligned separately to a reference genome using the HISAT2 software in the orientation mode (<http://ccb.jhu.edu/software/hisat2/index.shtml>). The mapped reads for each sample were assembled using StringTie (<https://ccb.jhu.edu/software/stringtie/index.shtml?t=example>) in a reference-based approach.

The expression level of each transcript was calculated using the TPM or FPKM method to identify differentially expressed genes (DEGs) between two different samples. Gene abundances were quantified using RSEM (<http://deweylab.biostat.wisc.edu/rsem/>). Analysis of differential gene expression, KEGG pathway analysis, and Gene Set Enrichment Analysis (GSEA) were performed on the Majorbio I-Sanger Cloud platform (<https://cloud.majorbio.com>) or OmicStudio tools (<https://www.omicstudio.cn/tool>). The detailed RNA sequencing data have been deposited in NCBI's Gene Expression Omnibus (GEO) and can be accessed through the GEO series accession number GSE234120 and GSE234122.

2.24. DNA constructs

Human *PIM1* and *HDAC2* were amplified by PCR and cloned to a pITA vector with C-terminal 3 × FLAG tag or N-terminal 6 × MYC tag. Human *HDAC2* was amplified by PCR and cloned to pET-28a(+) vector (Novagen, Madison, WI, USA) with N-terminal 6 × MYC tag to produce recombinant MYC-tagged *HDAC2* proteins. The primer sequences are listed in Table S2.

Anti-*PIM1* shRNAs were designed based on the pLKO.1 vector. Potential target sites in *PIM1* were located using siRNA Target Finder software (Ambion, USA). To design highly effective plasmid-based shRNA constructs, the shRNA target sequences were also checked for 100% homology against the complete genomic sequences of *PIM1* strains. The sequences of the siRNAs are listed in Table S2.

2.25. DNA transfection

The constructed plasmid pITA-FLAG-*PIM1*, pITA-6xMYC-*HDAC2*, pLKO.1-*shPIM1*#1, and pLKO.1-*shPIM1*#2 were transfected into 293T cells in addition with assistant vectors psPAX2 and pMD2.G. Forty-eight hours after transfection, the viral supernatants were harvested and filtered to remove cell debris. The mixture of viral supernatants and the medium was incubated with Caco2 cells for 12 h after the centrifugation at 1800×g (Eppendorf Centrifuge 5810R) for 45 min at 20 °C. The Caco2 cells infected with the virus were then selected by drug treatment.

2.26. Recombinant protein purification

The overexpression plasmid pET-28a(+)-MYC-*HDAC2* was transformed into the BL21 (DE3) cells for induction and expression. The bacteria were cultured in LB broth at 37 °C until an OD600 of 0.6–0.8. Protein expression was induced by 0.1 mmol/L isopropyl β-D-thiogalactopyranoside (IPTG, B300845, Sangon Biotech, Shanghai, China) at 16 °C for 18 h. Cultured bacteria were harvested by centrifugation at 8000×g (Eppendorf Centrifuge 5810R) for 5 min at 4 °C. Cells were lysed with

sonication in a lysis buffer containing 50 mmol/L Tris-HCl pH 7.5, 100 mmol/L NaCl, and 10 μg/μL lysozyme (L6876, Sigma-Aldrich) and supplemented with a complete EDTA-free protease inhibitor cocktail (11697498001, Roche, Mannheim, Germany). The protein-containing supernatants were collected by centrifugation at 8000×g (Eppendorf Centrifuge 5810R) for 30 min at 4 °C. The protein was purified and eluted using the Ni-NTA Purification System (L00250, GenScript, Nanjing, China) following the manufacturer's instructions. The His-tagged protein was concentrated using Amicon Ultra-15 Centrifugal Filter Units (UFC903096, Millipore, Burlington, MA, USA) after dialysis against PBS. Protein concentration was determined spectrophotometrically using the BCA Protein Assay Kit (23225, Thermofisher Scientific), and proteins were visualized by Coomassie blue staining (CW0023, CWBio).

The recombinant plasmid pITA-FLAG-*PIM1* was overexpressed in 293T cells to purify the FLAG-tagged *PIM1* protein. The cell pellets were lysed using a lysis buffer containing 2 mmol/L EDTA, 50 mmol/L Tris-HCl pH 7.4, 150 mmol/L NaCl, 1% NP-40, 20% glycerol, and complete mini-EDTA-free protease inhibitor cocktail tablets. The protein-containing supernatant was incubated with anti-FLAG beads (A7470, Sigma-Aldrich) at 4 °C for 12 h with constant rotation. The beads were then incubated with FLAG peptides (M2435, Sigma-Aldrich) in TBS buffer (20 mmol/L Tris-HCl pH 7.6, 140 mmol/L NaCl) on ice for 2 h, followed by centrifugation to collect the recombinant FLAG-tagged proteins. Protein concentration was determined using a Nanodrop-2000 spectrophotometer and the BCA Protein Assay Kit (23225, Thermofisher Scientific).

2.27. In vivo kinase assay

For analysis of *HDAC2* phosphorylation, cells were lysed in RIPA lysis buffer (R0020, Solarbio) with the addition of protease inhibitors and phosphatase inhibitors. Whole-cell lysates supernatants were incubated with anti-MYC beads (A7470, Sigma-Aldrich) overnight at 4 °C. After incubation, beads were thoroughly washed with lysis buffer, boiled in SDS loading buffer and subjected to SDS-PAGE and Western blotting with anti-phosphoserine (ab9332, Abcam), or anti-phosphothreonine (ab9337, Abcam) antibodies.

2.28. In vitro pull-down assay

Recombinant FLAG-*PIM1* protein (1 μg) and recombinant MYC-*HDAC2* protein (1 μg) were incubated in binding buffer (20 mmol/L Tris-HCl pH 7.4, 0.1% Triton-X 100, 100 mmol/L NaCl, 20% glycerol, 1% BSA) for 12 h. The mixture was then added to anti-FLAG beads (A2220, Sigma-Aldrich) and incubated for another 12 h at 4 °C with constant rotation. After washing, the beads were boiled in SDS loading buffer and analyzed by SDS-PAGE and Western blotting.

2.29. TCGA data analysis

The relationship between the incidence of colorectal cancer and the *PIM1* gene expression was analyzed by The Cancer Genome Atlas (TCGA) database. The Kaplan-Meier survival of colorectal cancer patients with different *PIM1* gene expression levels was analyzed by OncoLnc at <http://www.oncolnc.org>.

2.30. AOM/DSS-induced CAC in mice

Six–eight-week-old mice were intraperitoneally injected with 10 mg/kg AOM (MP Biomedicals). Seven days after the AOM intervention, the mice received drinking water containing 2% DSS for seven consecutive days. Mice were then provided regular drinking water for 14 days, and the same cycle was repeated twice, followed by normal drinking water until Day 70. All mice were sacrificed, and the colon was collected and cut open longitudinally. The presence of visible tumors was assessed, and the number of tumor nodules was quantified. Additionally, the samples were fixed in 4% paraformaldehyde for histopathological examination.

2.31. ChIP-seq

To prepare the ChIP-Seq library, 2×10^6 Caco2 cells underwent crosslinking with 1% formaldehyde for 10 min at room temperature. The crosslinking reaction was then quenched by adding 125 mmol/L glycine. The chromatin was fragmented, and the resulting fragments were subjected to pre-clearing. Immunoprecipitation was carried out using Protein A + G Magnetic beads coupled with antibodies specific to anti-HDAC2 (ab7029, Abcam). After reverse crosslinking, the ChIP and input DNA fragments were processed for end repair and A-tailing using the NEBNext End Repair/dA-Tailing Module (E7442, NEB). Subsequently, adaptor ligation was performed using the NEBNext Ultra Ligation Module (E7445, NEB). The DNA libraries were amplified through 15 cycles of PCR and sequenced using Illumina Hi-Seq with paired-end 2×150 sequencing mode.

Raw reads were filtered to obtain high-quality clean reads by removing sequencing adapters, short reads (length <35 bp), and low-quality reads using Cutadapt v1.18 and Trimmomatic v0.38. Then FastQC (with default parameters) ensures high read quality. The clean reads were mapped to the human genome (assembly GRCh38) using the Bowtie2 v2.3.4.1 (with default parameters) software. Duplicate reads were then removed using Picard MarkDuplicates. Peak detection was performed using the MACS v2.1.2. Annotation of peak sites to gene features was performed using the ChIPseeker R package. The detailed ChIP-seq data have been deposited in NCBI's Gene Expression Omnibus (GEO) and can be accessed through the GEO series accession number GSE234117.

2.32. ChIP-qPCR

ChIP assay was performed as described previously³⁰. The immunoprecipitation from Caco2 cells was performed using the anti-HDAC2 antibody (ab7029, Abcam). The precipitated DNA fragments were purified and analyzed by real-time PCR with the related primers. The primer sequences are listed in Table S2.

2.33. Statistical analysis

Data were presented as the mean \pm standard deviation (SD). The statistical significance was determined by unpaired Student's *t*-test, paired Student's *t*-test, one-way ANOVA, or two-way ANOVA. The correlation was analyzed with Pearson correlation. Statistical analyses were performed using GraphPad Prism 6 (San Diego, CA, USA).

3. Results

3.1. PIM1 is elevated in the colonic tissues of patients and mice with colitis

To investigate the molecular mechanisms of PIM1 in ulcerative colitis, the protein levels of PIM1 were measured in colonic biopsies from healthy controls and patients with mild and severe UC. We found that PIM1 protein levels were significantly elevated in colon tissues from colitis samples compared to healthy controls. Higher PIM1 expression was observed in colonic tissues from severe UC than from mild UC (Fig. 1A). Accordingly, there was a positive correlation between PIM1 protein levels and the erythrocyte sedimentation rate (a widely used serum biomarker for UC) (Fig. 1B). Using the Gene Expression Omnibus (GEO) database (GSE75214, GSE65114, and GSE47908), it was further confirmed that PIM1 expression was higher in ulcerative colitis specimens than in healthy controls (Fig. 1C).

Next, we wanted to determine PIM1 protein levels in colon tissues from DSS-induced colitis in mice. Consistent with the previous findings²², PIM1 expression was markedly increased in colonic tissues of DSS-treated mice (Fig. 1D and E). Notably, PIM1 was predominantly expressed in the colonic epithelia of UC patients and DSS-treated mice (Fig. 1A and D). We further validated this observation using single-cell RNA sequencing (scRNA-seq) data from colon biopsies of healthy controls and UC patients (Single Cell Portal accession SCP259)³¹ (Supporting Information Fig. S2A). Then, we investigated whether intestinal microbiota influenced PIM1 expression. Wild-type mice were administered a cocktail of antibiotics (Abx) in drinking water before the DSS challenge. Abx treatment attenuated PIM1 expression induced by DSS (Fig. 1F and Fig. S2B). Meanwhile, we performed the fecal microbiota transplantation from colitis/WT mice into WT mice. PIM1 expression was higher in colonic tissues of colitis microbiota recipient mice (Fig. 1G). These results indicated intestinal microbiota is required for DSS-induced PIM1 expression in mice. Together, these results suggest a potential association between PIM1 and UC pathogenesis.

3.2. *Pim1*^{+/-} mice exhibit resistance to DSS-induced colitis

To investigate whether PIM1 contributes to UC pathogenesis, we generated heterozygous *Pim1*^{+/-} and homozygous *Pim1*^{-/-} mice, which were verified using immunoblot and immunohistochemical analysis (Fig. S2C and S2D). Histological evaluation of the colon revealed no significant changes in *Pim1*^{+/-} mice, *Pim1*^{-/-} mice, and WT mice (Fig. S2E). In line with previous studies³², *Pim1*^{-/-} mice exhibited overall growth retardation compared with *Pim1*^{+/-} and WT mice (Fig. S2F). Similarly, the colon length was significantly altered in *Pim1*^{-/-} mice compared to *Pim1*^{+/-} mice and WT mice (Fig. S2G), indicating the limited subsequent investigations in *Pim1*^{-/-} mice. Therefore, we evaluated the physiological roles of PIM1 in acute DSS-induced colitis using *Pim1*^{+/-} mice. *Pim1*^{+/-} mice showed lower body weight loss and disease activity index (DAI, a clinical disease score to assess the clinical symptoms of colitis) compared with WT littermates (Fig. 2A and B). Meanwhile, *Pim1*^{+/-} mice displayed longer colon length and less histological damage than WT littermates (Fig. 2C and D). This phenotype was accompanied by increased goblet cells and elevated expression of the goblet cell marker

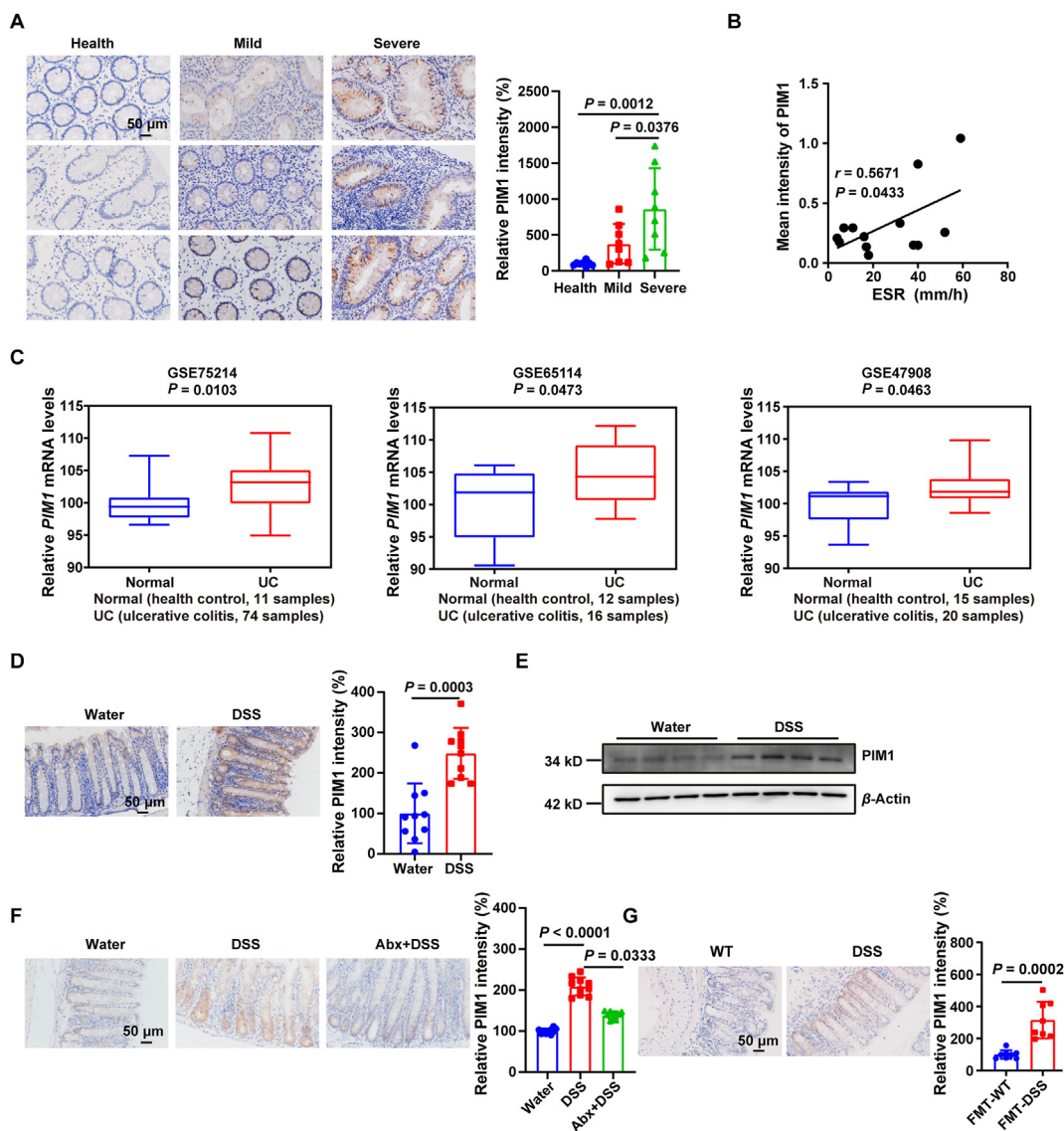


Figure 1 PIM1 is upregulated in the colon tissue of UC patients and mice with colitis. (A) Immunohistochemistry staining and quantitation of PIM1 in the colon tissue samples from healthy controls ($n = 9$) and patients with mild UC ($n = 8$) and severe UC ($n = 8$). (B) Pearson's correlation analysis between the PIM1 expression of colonic biopsies and ESR (erythrocyte sedimentation rate) from 13 patients with UC (Spearman's rank correlation coefficient, $r = 0.5671$, statistical analysis is performed using linear regression, $P = 0.0433$). (C) Box plot of *PIM1* mRNA expression in healthy controls and UC patients from the GEO database. (D) Immunohistochemistry staining and quantitation of PIM1 in the colon tissue from wild-type mice with or without DSS treatment. $n = 10$ from 3 independent experiments. (E) Western blotting of PIM1 expression in the colon tissue from mice without or with DSS treatment ($n = 4$). (F, G) Immunohistochemistry staining and quantitation of PIM1 in the colon tissue from the indicated mice ($n = 10$ from 3 independent experiments). Scale bar: 50 μm . The data represent the mean \pm SD. Statistical significance was determined by one-way ANOVA (A, F) or unpaired Student's *t*-test (C, D, and G).

MUC2 (essential factors in the clinical manifestations of colitis) (Fig. 2E and F). In addition, permeability assays validated that *Pim1*^{+/-} mice maintained better intestinal barrier function than WT littermates (Fig. 2G).

As UC pathogenesis is associated with intestinal inflammation¹, we then assessed whether PIM1 deficiency would alter the state of intestinal inflammation. The mRNA levels of pro-inflammatory cytokines and chemokines, including *Tnfa*, *iNOS*, *Il-1 β* , *Il-6*, *Ccl2*, and *Cxcl1*, were substantially diminished in colon tissues of *Pim1*^{+/-} mice compared with WT littermates (Fig. 2H). Consistent with intestinal inflammation, *Pim1*^{+/-} mice had lower immune cell infiltration, including dendritic cells,

macrophages, and neutrophils in the colonic lamina propria (cLP). Meanwhile, a lower percentage of Th1, Th2, and Th17 cells and a higher percentage of Treg cells in mesenteric lymph nodes (MLN) were observed in *Pim1*^{+/-} mice (Fig. 2I and Fig. S2H). Overall, these findings indicate that PIM1 deficiency protects against DSS-induced colitis.

3.3. *PIM1* deficiency alters colonic goblet cell differentiation

To determine how PIM1 deficiency affects colitis, the functions of PIM1 in epithelial homeostasis under the naive condition were evaluated. We discovered that LGR5 expression (the intestinal

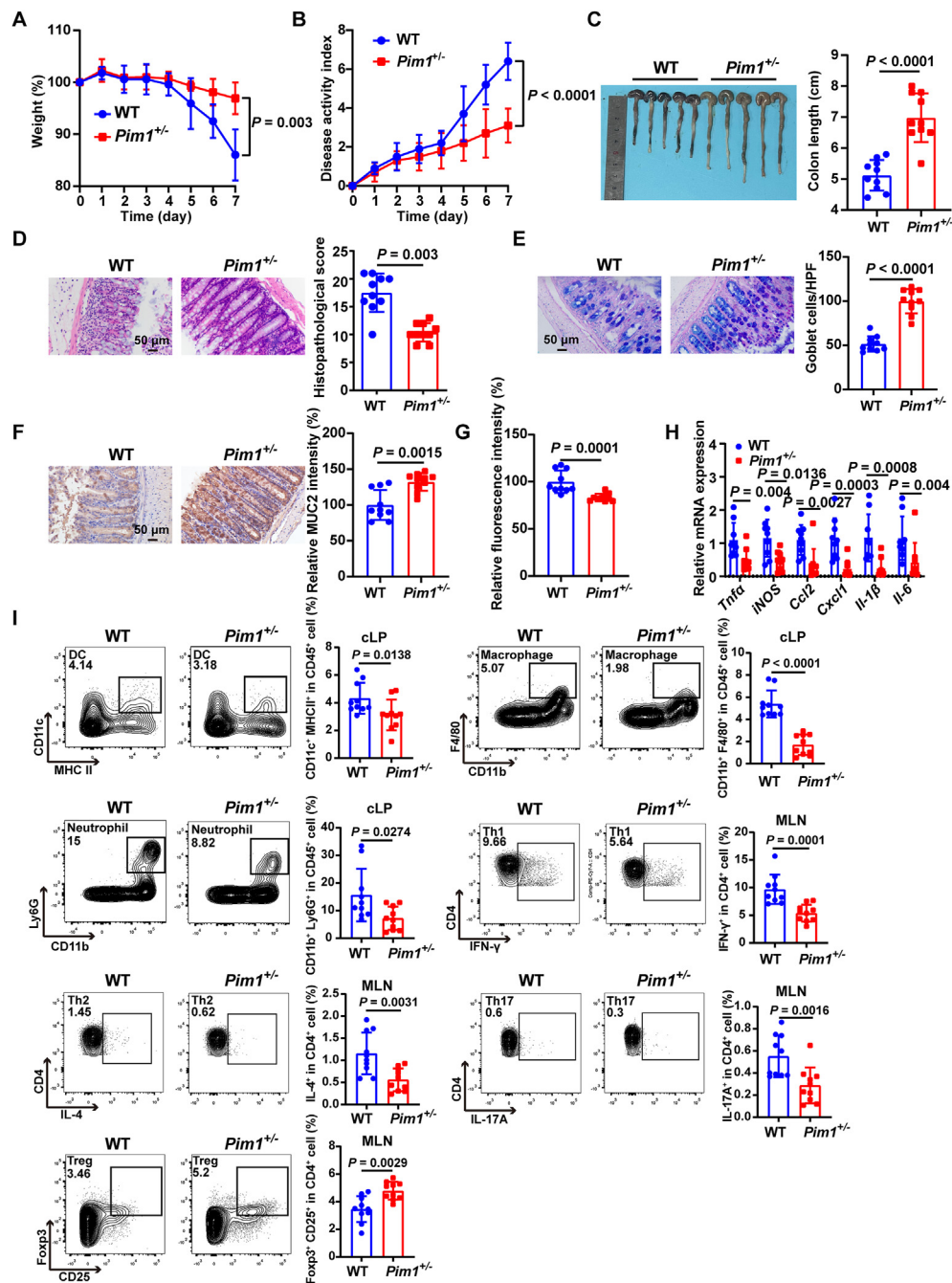


Figure 2 PIM1 deficiency attenuates DSS-induced colitis symptoms. (A–F) WT and *Pim1*^{+/-} mice were administered 1.5% DSS in drinking water for 7 days to induce colitis ($n = 10$ from 3 independent experiments). (A) Body weight loss of WT and *Pim1*^{+/-} mice. (B) Disease activity index of WT and *Pim1*^{+/-} mice. (C) Measurement and quantification of colon length in WT and *Pim1*^{+/-} mice. (D) Representative H&E staining of colons and quantitation of histologic scores in colonic sections from DSS-challenged WT and *Pim1*^{+/-} mice. (E) Alcian blue-Periodic acid Schiff (AB-PAS; goblet cells) staining and quantitation in colonic sections from DSS-challenged WT and *Pim1*^{+/-} mice. (F) Immunohistochemistry staining and quantitation of MUC2 in colonic sections from DSS-challenged WT and *Pim1*^{+/-} mice. (G) Fluorescein isothiocyanate (FITC)-dextran measurement in plasma from WT and *Pim1*^{+/-} mice at day 6 post-DSS treatment ($n = 10$ from 3 independent experiments). (H) Real-time PCR analysis of mRNA levels of the indicated proinflammatory cytokines in the colon tissue from DSS-challenged WT and *Pim1*^{+/-} mice ($n = 9$ from 3 independent experiments). (I) Representative flow cytometry analysis of the indicated cells (left) and percentage (right) of indicated cells in mesenteric lymph nodes (MLN) and colonic lamina propria (cLP) from DSS-challenged WT and *Pim1*^{+/-} mice ($n = 10$ from 3 independent experiments). Scale bar: 50 μ m. The data represent the mean \pm SD. Statistical significance was determined by two-way ANOVA (A, B) or unpaired Student's *t*-test (C–I).

stem cell marker) is similar in *Pim1*^{+/-} mice colon tissues and WT littermates (Supporting Information Fig. S3A). We next examined whether PIM1 deficiency altered epithelial differentiation patterns. PIM1 deficiency increased goblet cell numbers in colons of *Pim1*^{+/-} mice (Fig. S3B). Consistent with an increase in goblet cells, the MUC2 protein level and thickness of the mucus layer were elevated in *Pim1*^{+/-} mice (Fig. S3C and S3D). Considering that tight junctions are essential for epithelial barrier function and that aberrant modulation of tight junctions contributes to UC pathogenesis^{33,34}, we assessed whether PIM1 deficiency maintains the barrier integrity by regulating tight junction proteins. Nevertheless, the tight junction proteins OCCLUDIN and ZO-1 expression did not differ in *Pim1*^{+/-} mice (Fig. S3E and S3F). To address whether PIM1 deficiency affects the regeneration capacity of epithelium, cell proliferation using Ki-67 staining and cell apoptosis using cleaved caspase-3 staining were examined. The numbers of Ki-67 positive cells were significantly higher in *Pim1*^{+/-} mice, while cleaved caspase-3 positive cells in *Pim1*^{+/-} mice were comparable to those of WT mice (Fig. S3G and S3H).

To validate the functions of PIM1 in epithelial cells *in vitro*, we performed the PIM1 knockdown and overexpression in human colorectal cancer cell line Caco2. In line with the *in vivo* results, Caco2 cells with PIM1 knockdown displayed higher MUC2 expression (Fig. S3I). Accordingly, MUC2 expression was significantly reduced in Caco2 cells with PIM1 overexpression (Fig. S3J). These data indicate that PIM1 deficiency contributes to epithelial homeostasis by promoting goblet cell differentiation and regeneration.

3.4. Epithelial PIM1 confers increased susceptibility to DSS-induced colitis

To determine whether the phenotypes observed in PIM1-deficient mice were of epithelial origin, we developed *Pim1*^{K1}Villin-Cre mice, allowing for IEC-specific PIM1 overexpression, which was confirmed by immunohistochemical staining (Supporting Information Fig. S4A). The growth rate and body size of WT and *Pim1*^{K1}Villin-Cre mice appeared identical (Fig. S4B). In addition, we observed no difference in histological evaluation and colon length between WT and *Pim1*^{K1}Villin-Cre mice (Fig. S4C and S4D).

Next, we examined the phenotypes of *Pim1*^{K1}Villin-Cre mice with DSS treatment. In accordance with results obtained using *Pim1*^{+/-} mice, *Pim1*^{K1}Villin-Cre mice exhibited profound weight loss, greater disease activity index, exacerbated colonic shortening, and more histologically severe damage than WT mice (Fig. 3A–D). Histological and immunohistochemical analysis revealed that the goblet cell numbers and MUC2 protein levels were strikingly decreased in colons of *Pim1*^{K1}Villin-Cre mice compared with WT mice (Fig. 3E and F). Additionally, the permeability for FITC-Dextran was substantially upregulated in *Pim1*^{K1}Villin-Cre mice (Fig. 3G). Furthermore, colonic mRNA levels of *iNOS*, *Il-1β*, *Il-6*, *Tnfrα*, *Ccl2*, and *Cxcl1* increased significantly in *Pim1*^{K1}Villin-Cre mice (Fig. 3H). Consistently, an intense infiltration of dendritic cells, macrophages, and neutrophils was observed in *Pim1*^{K1}Villin-Cre mice (Fig. 3I). The percentage of Th1, Th2, and Th17 cells was also slightly increased in *Pim1*^{K1}Villin-Cre mice, but without statistical differences (Fig. 3I). Meanwhile, the lower percentage of Treg cells was observed in *Pim1*^{K1}Villin-Cre mice (Fig. 3I).

Based on the homeostatic changes observed in *Pim1*^{+/-} mice, we asked whether epithelial PIM1 overexpression contributes to

epithelial homeostasis disruption. The numbers of goblet cells and the MUC2 levels were reduced in *Pim1*^{K1}Villin-Cre mice in the basal state using immunohistochemical staining (Fig. S4E and S4F). This phenotype was accompanied by decreased Ki-67 positive proliferating epithelial cells in *Pim1*^{K1}Villin-Cre mice (Fig. S4G). Collectively, these findings reveal that epithelium-intrinsic PIM1-induced disruption of epithelial homeostasis is responsible for the susceptibility to DSS-induced colitis.

3.5. *Pim1*^{+/-} mice protect against colitis in a microbiota-independent manner

Intestinal microbiota plays a crucial role in colitis. Intestinal microbiota can mainly affect the bioavailability of oral drugs by changing the metabolism catalyzed by intestinal microbial enzymes, regulating host gene expression and substrate competition, and affecting intestinal properties³⁵. Given that PIM1 expression can be regulated by intestinal microbiota (Fig. 1F and G), we investigated the function of intestinal microbiota in the protective colitis phenotype of *Pim1*^{+/-} mice. We performed 16S rDNA sequencing of *Pim1*^{+/-} and WT mice stool samples. Neither the amount of bacterial DNA nor the Shannon diversity index differed significantly between *Pim1*^{+/-} and WT mice (Supporting Information Fig. S6A and S6B). However, *Pim1*^{+/-} mice displayed significant β -diversity differences in the microbial composition (Fig. S6C). In addition, *Pim1*^{+/-} mice possessed a greater relative abundance of *Roseburia*, *Alloprevotella*, and *Bifidobacterium* at the genus level (Fig. S6D, S6E and S6H), which are implicated in protection from colitis. Thus, these findings demonstrate that PIM1 deficiency altered gut microbiota composition.

Then, we investigated whether distinct intestinal microbiota contributes to *Pim1*^{+/-} mice resistance to DSS-induced colitis. We administered *Pim1*^{+/-} and WT mice with broad-spectrum antibiotics to deplete their intestinal microbiota, followed by a DSS challenge (Supporting Information Fig. S5A). Antibiotic treatment did not eliminate the difference in disease activity index, colon length, and histological scores between *Pim1*^{+/-} and WT mice (Fig. S5B–S5D). Meanwhile, we cohoused WT with *Pim1*^{+/-} mice for four weeks before DSS treatment (Fig. S5E). Cohoused *Pim1*^{+/-} mice continued to exhibit mild colitis compared with cohoused WT mice (Fig. S5F–S5H). Consistently, the number of goblet cells and Ki-67 positive epithelia, as well as the MUC2 level, were persistently increased in cohoused *Pim1*^{+/-} mice (Fig. S5I–S5K). The intestinal microbial composition of *Pim1*^{+/-} and WT mice after cohousing was analyzed. The amount of bacterial DNA, Shannon diversity, and β -diversity showed no significant differences in the feces of cohoused *Pim1*^{+/-} and WT mice (Fig. S6A–S6C), and the gut microbiota of cohoused WT mice displayed a significant shift toward that of cohoused *Pim1*^{+/-} mice compared with single-housed WT mice (Fig. S6D–S6H). In summary, these data indicate that PIM1 deficiency alters the gut microbiota composition, which is dispensable for protection against colitis in *Pim1*^{+/-} mice.

3.6. PIM1 deficiency promotes goblet cell differentiation through regulating Wnt and Notch signaling

To provide insight into the molecular mechanisms underlying intestinal epithelial alterations in *Pim1*^{+/-} mice, gene expression alterations in IECs from WT and *Pim1*^{+/-} mice were characterized using RNA-seq. The results showed that 1434 genes were

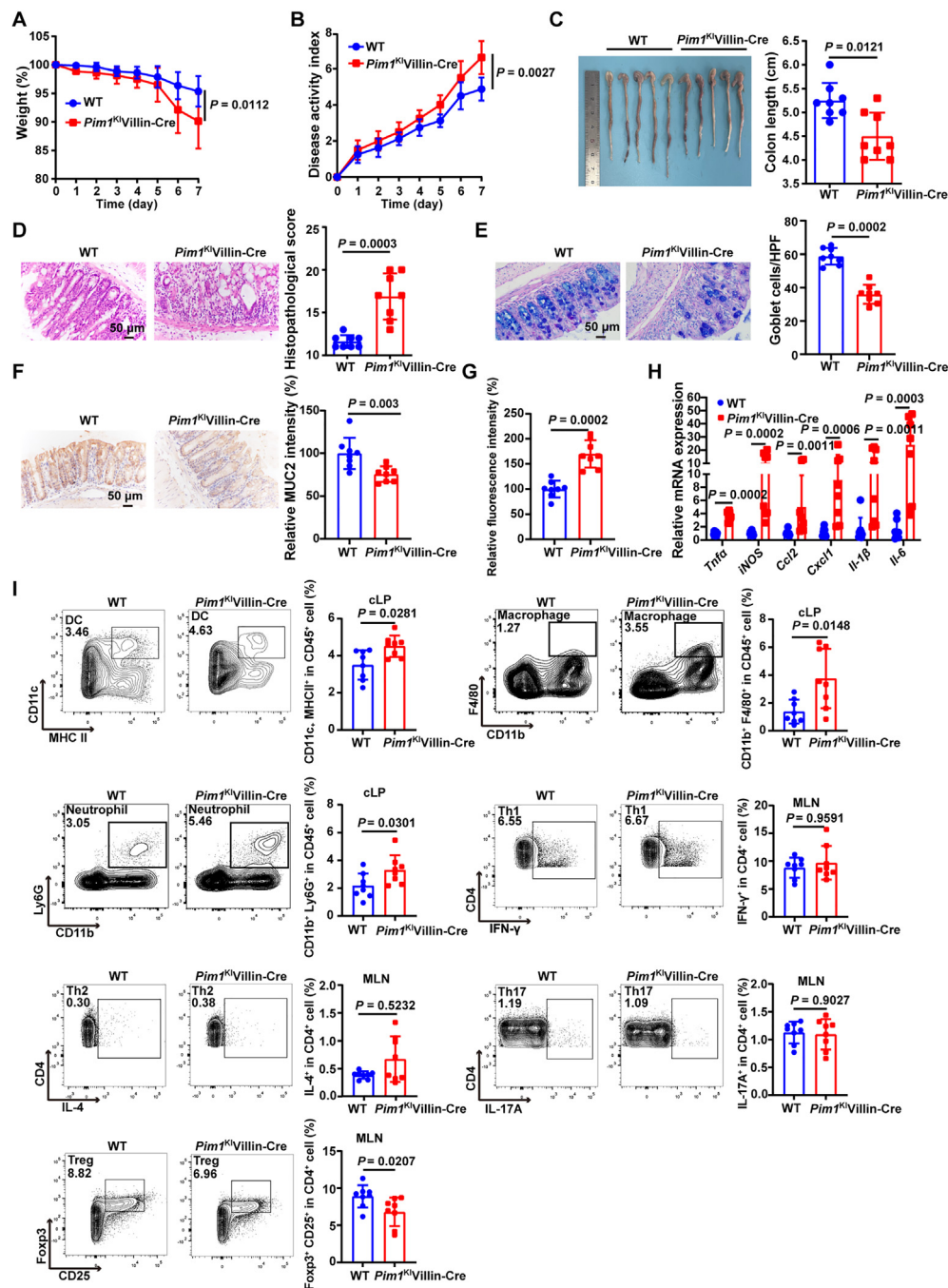


Figure 3 Epithelial PIM1 overexpression promotes susceptibility to DSS-induced colitis. (A–F) WT and *Pim1*^{K1}Villin-Cre mice were administered 1.5% DSS in drinking water for 7 days ($n = 8$ from 2 independent experiments). (A) Body weight loss of DSS-treated WT and *Pim1*^{K1}Villin-Cre mice. (B) Disease activity index of DSS-treated WT and *Pim1*^{K1}Villin-Cre mice. (C) Measurement and quantification of colon length in DSS-treated WT and *Pim1*^{K1}Villin-Cre mice. (D) Representative H&E staining of colons and quantitation of histologic scores in colonic sections from DSS-challenged WT and *Pim1*^{K1}Villin-Cre mice. (E) AB-PAS staining and quantification in colonic sections from DSS-challenged WT and *Pim1*^{K1}Villin-Cre mice. (F) Immunohistochemistry staining and quantitation of MUC2 in colonic sections from DSS-challenged WT and *Pim1*^{K1}Villin-Cre mice. (G) FITC-dextran measurement in plasma from WT and *Pim1*^{K1}Villin-Cre mice on Day 6 post DSS treatment ($n = 8$ from 2 independent experiments). (H) Real-time PCR analysis of the relative mRNA levels of the indicated genes in the colon tissues from DSS-challenged WT and *Pim1*^{K1}Villin-Cre mice ($n = 8$ from 2 independent experiments). (I) Representative flow cytometry analysis of the indicated cells (left) and percentage (right) of indicated cells in MLN and cLP from DSS-challenged WT and *Pim1*^{K1}Villin-Cre mice ($n = 8$ from 2 independent experiments). Scale bar: 50 μ m. The data represent the mean \pm SD. Statistical significance was determined by two-way ANOVA (A, B) or unpaired Student's *t*-test (C–I).

upregulated and 1518 genes were downregulated in *Pim1*^{+/-} mice ($P < 0.05$ and fold change > 1.5) (Fig. 4A). These genes include goblet cell-related and differentiation-determining genes (Fig. 4A, marked genes). Consistently, KEGG analysis revealed that the downregulated genes in IECs from *Pim1*^{+/-} mice were

significantly enriched in FoxO, MAPK, Wnt, TNF, Notch, and JAK-STAT signaling pathways (Fig. 4B). Of them, Wnt and Notch signaling downregulation promotes intestinal goblet cell differentiation. The expression levels of goblet cell markers including *Muc4*, *Clca1*, and *Muc3a* were upregulated in PIM1-

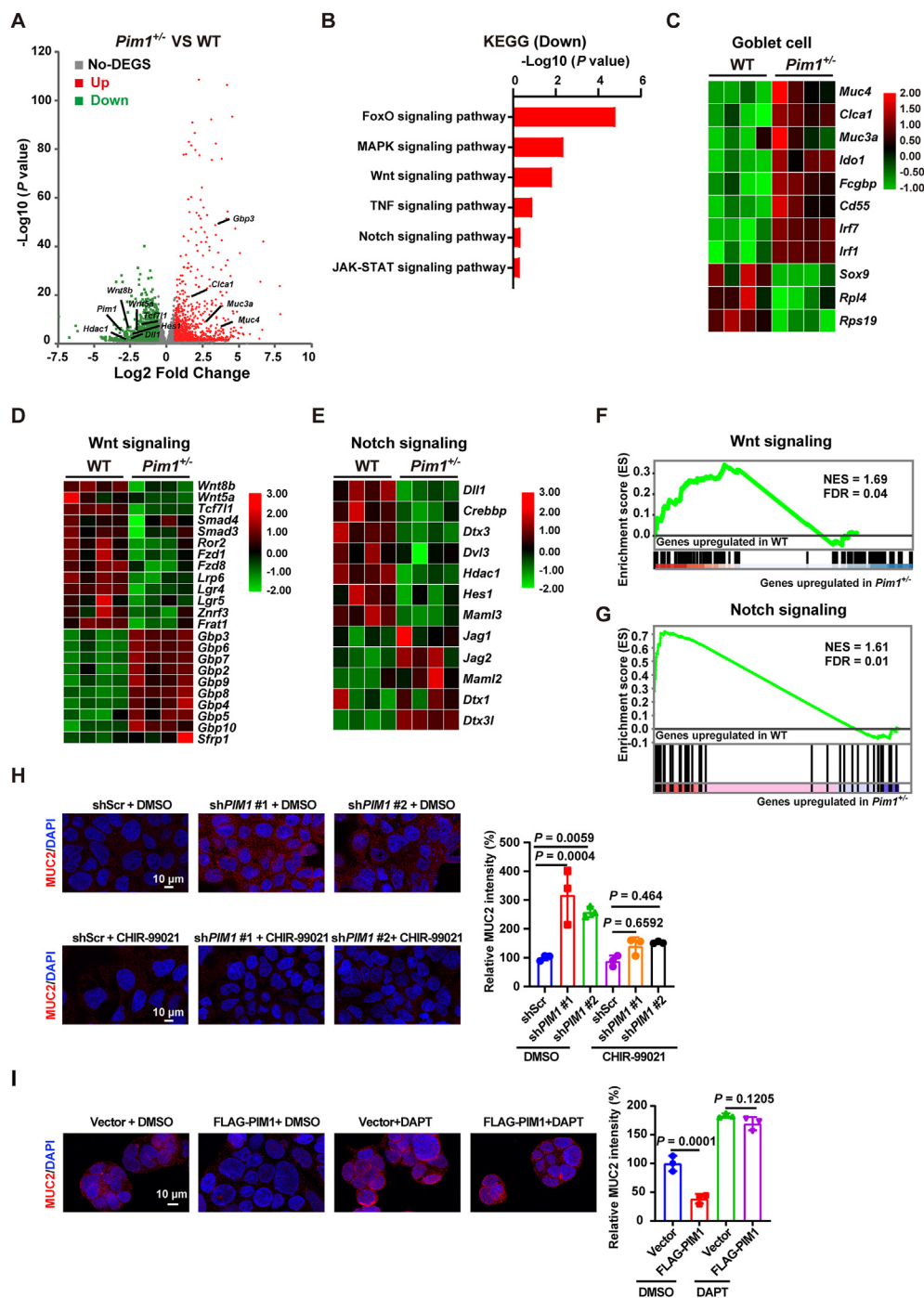


Figure 4 PIM1 deficiency results in down-regulation of the Wnt and Notch signaling pathways. (A–G) Transcriptomic profiling of IECs from WT and *Pim1*^{+/-} mice ($n = 4$ for each genotype). (A) Volcano plot displaying the differentially expressed genes in IECs from *Pim1*^{+/-} mice compared with WT mice. Red indicates up-regulated genes; green indicates down-regulated genes; gray indicates non-differentially expressed genes (No-DEGS). (B) KEGG analysis of downregulated genes in IECs from *Pim1*^{+/-} mice. (C) Heatmap depicting the relative expression of goblet cell signature genes. (D, E) Heatmap showing the relative expression of Wnt (D) and Notch (E) signaling pathway-related genes. (F, G) GSEA analysis showing enrichment of the Wnt (F) and Notch (G) signaling pathway gene set. (H, I) Representative confocal images and quantification of MUC2 staining (red) and DAPI (blue) in Cac2 cells as indicated ($n = 3$ from 3 independent experiments). Scale bar: 10 μ m. The data represent the mean \pm SD. Statistical significance was determined by one-way ANOVA (H, I).

deficient IECs (Fig. 4C). Wnt signaling-related genes such as *Wnt8b*, *Wnt5a*, *Tcf7l1*, *Fzd1*, and *Lrp6* and Notch signaling-related genes such as *Dll1*, *Hes1*, and *Dvl3* were downregulated in PIM1-deficient IECs (Fig. 4D and E). Furthermore, gene set enrichment analysis (GSEA) confirmed that Wnt and Notch signaling pathways were strikingly down-regulated in IECs from *Pim1*^{+/-} mice (Fig. 4F and G). To substantiate this observation, we performed whole-transcriptome RNA-seq in PIM1-overexpressing Caco2 cells. The results showed that 356 genes were upregulated and 498 genes were downregulated in PIM1-overexpressing Caco2 cells ($P < 0.05$ and fold change > 1.5 , Supporting Information Fig. S7A). In line with RNA-seq analysis *in vivo*, the expression levels of goblet cell markers, including *MUC2*, *MUC4*, and *MUC13*, were downregulated in PIM1-overexpressing Caco2 cells (Fig. S7B). The Wnt and Notch signaling were enriched in the upregulated genes in PIM1-overexpressing Caco2 cells (Fig. S7C). Wnt and Notch signaling pathways were consistently activated in PIM1-overexpressing Caco2 cells (Fig. S7D and S7E).

To further elucidate the role of Wnt and Notch signaling pathways in the regulation of PIM1-induced goblet cell differentiation, we performed rescue assays by treatment of PIM1-knockdown Caco2 or PIM1-overexpressing Caco2 cells with Wnt activator CHIR99021 and Notch inhibitor DAPT, respectively. CHIR99021 treatment significantly restored the upregulated MUC2 expression in PIM1-knockdown cells, and DAPT treatment significantly rescued the decreased MUC2 levels in PIM1-overexpression cells (Fig. 4H and I). These data indicate that PIM1 enhances goblet cell differentiation by suppressing the Wnt and Notch signaling pathways.

3.7. PIM1 modulates goblet cell differentiation by downregulating HDAC2 expression

PIM1 is a serine/threonine kinase essential in multiple biological processes³⁶. To understand how PIM1 regulates Wnt and Notch signaling, we performed immunoprecipitation and mass spectrometry in Caco2 cells overexpressing FLAG-PIM1 to identify its target proteins. The identified PIM1-associated proteins included HDAC2 and other known PIM1-interacting proteins of such as DDX5 and EDC3 (Fig. 5A). To verify the interaction between PIM1 and HDAC2, Caco2 cells overexpressing FLAG-PIM1 and MYC-HDAC2 were subjected to co-immunoprecipitation, and FLAG-PIM1 was immunoprecipitated with MYC-HDAC2, and *vice versa* (Fig. 5B). To further investigate whether PIM1 interacted endogenously with HDAC2, co-immunoprecipitation with anti-HDAC2 antibody was performed in Caco2 cells and IECs with PIM1 overexpression, and PIM1 was detected in HDAC2 immunoprecipitates (Fig. 5C and Fig. S7F). Moreover, *in vitro* pulldown assay further demonstrated a direct interaction between PIM1 and HDAC2 (Fig. 5D). Additionally, proximity ligation assay revealed the colocalization of PIM1 and endogenous HDAC2 in Caco2 cells (Fig. 5E). In summary, these findings indicate that PIM1 directly interacts with HDAC2.

Due to the direct interaction of PIM1 with HDAC2, we hypothesized that PIM1 could phosphorylate HDAC2. Immunoprecipitation of HDAC2 followed by Western blotting analysis of phosphoserine and phosphothreonine confirmed that PIM1 phosphorylated the endogenous HDAC2 at serine and threonine (Fig. 5F and Fig. S7G). Simultaneously, PIM1-mediated phosphorylation of HDAC2 was further verified in IECs with PIM1 overexpression (Fig. S7H). As several studies have shown that HDAC2

phosphorylation promotes its degradation²⁴, we measured the expression of HDAC2 in Caco2 cells with PIM1 overexpression or knockdown by Western blotting and immunofluorescence. We found that PIM1 decreased the HDAC2 protein level (Fig. 5G and H, Fig. S7I and S7J).

To further support this observation, we examined HDAC2 expression in colon tissue from *Pim1*^{+/-} and *Pim1*^{K1}Villin-Cre mice. Immunohistochemical staining revealed that PIM1 attenuated the HDAC2 expression under basal and DSS-induced colitis conditions (Fig. 5I and J, Fig. S7K and S7L). Notably, the negative statistically significant correlation between PIM1 and HDAC2 expression was validated in colon tissues from ulcerative biopsies (Fig. 5K). Likewise, we observed the levels of *PIM1* negatively correlated with *HDAC2* expression among ulcerative colitis patients based on data from public databases (NCBI's Gene Expression Omnibus: GSE72514) (Fig. 5L).

We next investigated whether HDAC2 participates in PIM1-modulated goblet cell differentiation and found that HDAC2 overexpression essentially rescued the PIM1-induced MUC2 downregulation in Caco2 cells (Fig. 5M). Together, these results suggest that PIM1 suppressed HDAC2 protein level by phosphorylation, which induces PIM1-mediated goblet cell differentiation.

3.8. PIM1 affects Wnt signaling by regulating HDAC2 binding to the promoter of Wnt-related genes

To gain further mechanistic insights into the role of HDAC2 in PIM1-mediated goblet cell differentiation, we performed a ChIP-seq assay for HDAC2 in Caco2 cells overexpressing PIM1, focusing on the regions of HDAC2 binding of the transcription start site (TSS) and transcription end site (TES). The signal intensity of the HDAC2 peak was lower in PIM1-overexpressing Caco2 cells than in control cells (Fig. 6A and B). The ChIP-seq analysis generated 14,132 enriched regions (peaks), including 6688 unique control peaks and 2305 unique PIM1 peaks (Fig. 6C), and 55.7% of HDAC2 peaks decreased in the PIM1 group occurred within gene promoters (Fig. 6D). Using motif enrichment analysis of these decreased HDAC2 peaks, we identified two statistically significant motifs as potential HDAC2 binding sites in the promoter region of various genes to regulate gene expression (Fig. 6E). Furthermore, KEGG pathway analysis of these decreased HDAC2 peaks revealed a significant enrichment of Wnt signaling pathway (Fig. 6F). Visual analysis using IGV confirmed low enrichment of HDAC2 in the promoters of Wnt signaling-related genes such as *DVL1*, *LGR6*, *PRICKLE3*, *ROR1*, *SMAD3*, *NKD1*, *PRKCA*, *PRKCB*, and *FZD1* in the PIM1 group (Fig. 6G and Fig. S7M). ChIP-qPCR was used to verify the ChIP-seq results (Fig. 6H). In accordance with ChIP-seq results, the gene expression levels of these Wnt signaling-related genes were significantly higher in PIM1-overexpressing Caco2 cells using RNA-seq (Fig. 6I and J). These gene expression levels were consistently substantially decreased in PIM1-deficient IECs (Fig. 6K and L). These results demonstrate that the HDAC2-regulated Wnt signaling pathway partially accounts for PIM1-mediated goblet cell differentiation.

3.9. Upregulated PIM1 in epithelia accelerated AOM/DSS-induced CAC

Given that long-term chronic inflammation in UC patients has been recognized as a significant risk factor for colitis-associated

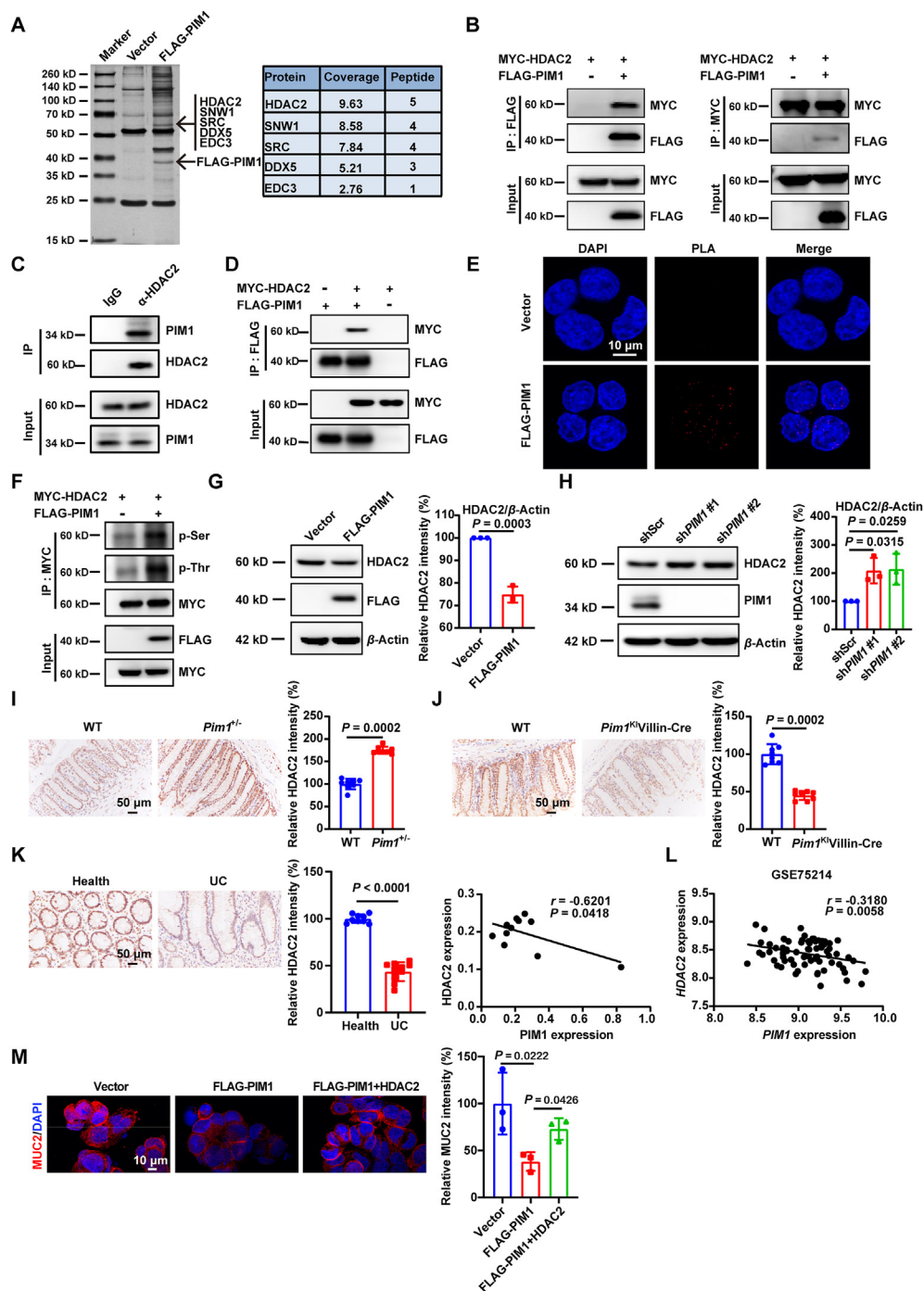


Figure 5 PIM1 alters goblet cell differentiation by downregulating HDAC2 expression. (A) Silver staining and mass spectrometry analysis of PIM1 binding proteins in the indicated Caco2 cells. (B) Co-IP analysis of the interactions between FLAG-PIM1 and MYC-HDAC2 in Caco2 cells. (C) Endogenous Co-IP analysis of the interactions between PIM1 and HDAC2 in Caco2 cells. (D) *In vitro* pull-down assay examining the interactions between FLAG-PIM1 and MYC-HDAC2. (E) Proximity ligation assay in Caco2 cells expressing FLAG-PIM1 or Vector. (F) Western blotting analysis of HDAC2 phosphorylation with anti-phosphoserine or anti-phosphothreonine antibodies after IP assay with anti-MYC antibody in Caco2 cells. (G, H) Western blotting analysis of the protein levels of HDAC2 in Caco2 cells infected with FLAG-PIM1 overexpression (G) or *PIM1* knockdown (H). The signal densities of HDAC2 in Caco2 cells were normalized to those of β -actin. Three independent experiments. (I) Immunohistochemistry staining and quantitation of HDAC2 in colonic sections from untreated WT and *Pim1*^{+/-} mice ($n = 10$ from 2 independent experiments). (J) Immunohistochemistry staining and quantitation of HDAC2 in colonic sections from untreated WT and *Pim1*^{KI}Villin-Cre mice ($n = 8$ from 2 independent experiments). (K) Immunohistochemistry staining and quantitation of HDAC2 using colonic biopsies from healthy controls ($n = 9$) and patients with UC ($n = 11$) (left). Pearson's correlation analysis between HDAC2 and PIM1 protein expression of colonic biopsies from 11 patients with UC (Spearman's rank correlation coefficient, $r = -0.6201$, statistical analysis is performed using linear regression, $P = 0.0418$) (right). (L) Pearson's correlation analysis between *HDAC2* and *PIM1* mRNA expression in intestinal biopsies of healthy controls and

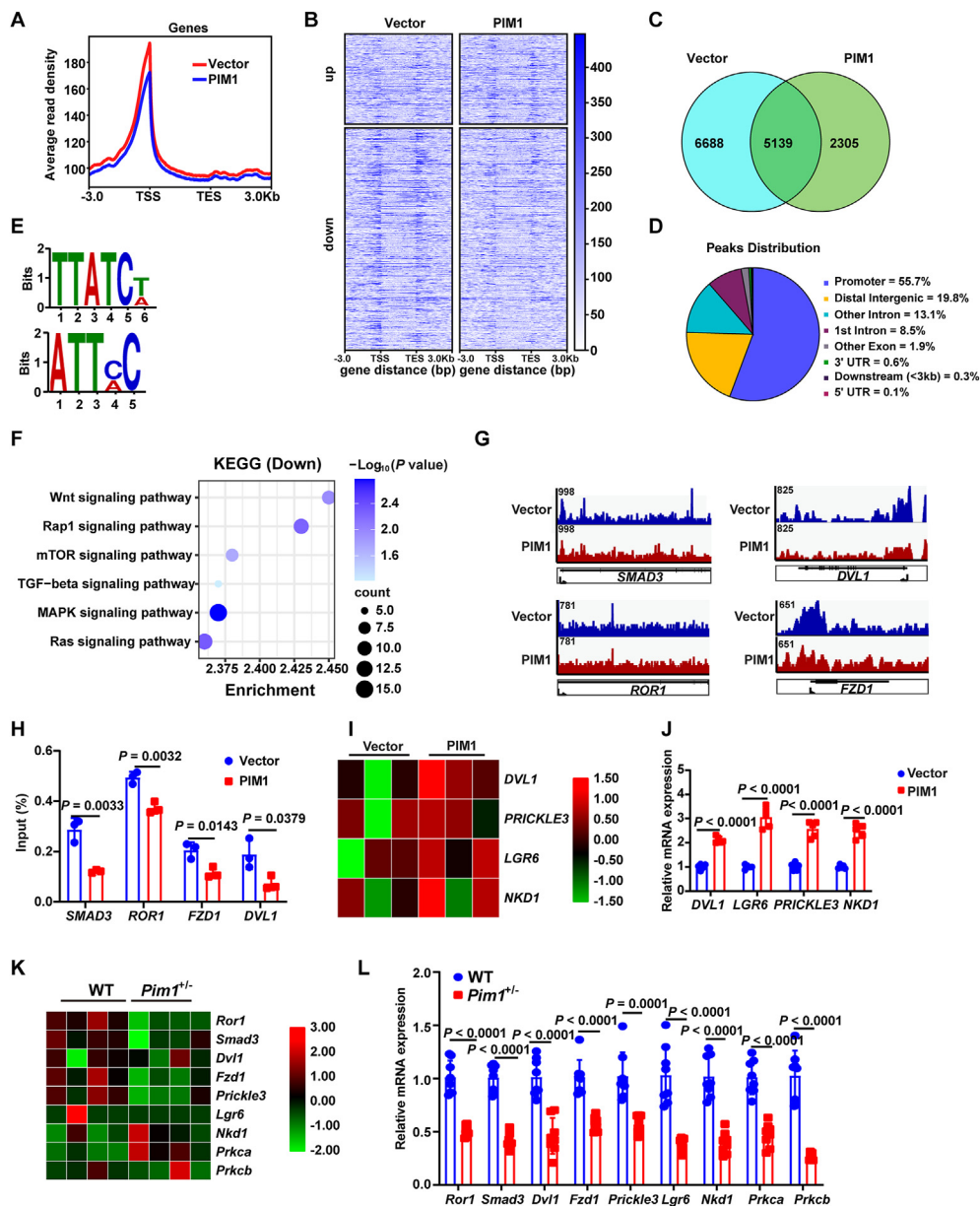


Figure 6 HDAC2 participates in PIM1-regulated goblet cell differentiation through the Wnt signaling pathway. (A–G) ChIP-seq analysis of HDAC2 in Caco2 cells infected with FLAG-PIM1 overexpression. (A) Aggregate plots of HDAC2 signals in the region -3 kb from the TSS to $+3$ kb from the TES. (B) Heatmap of HDAC2 peak signals with peaks subset into those upregulated (top) or downregulated (bottom) in the PIM1 group. (C) Venn diagram showing the number of HDAC2 unique peaks in the vector or PIM1 group. (D) Genome-wide distribution of differential HDAC2 peaks between the vector and PIM1 group. (E) DNA motif enrichment from downregulated HDAC2 peaks in the PIM1 group relative to the vector group. (F) KEGG analysis of downregulated genes in the PIM1 group. (G) Representative IGV tracks of Wnt signaling-related genes. (H) ChIP-qPCR analysis for HDAC2 at the promoter of Wnt signaling-related genes. (I) Heatmap showing the relative expression of Wnt signaling pathway-related genes in Caco2 cells with PIM1 overexpression. (J) Real-time PCR analysis of mRNA levels of Wnt signaling pathway-related genes in Caco2 cells with PIM1 overexpression ($n = 5$ from 3 independent experiments). (K) Heatmap showing the relative expression of Wnt signaling pathway-related genes in IECs from WT and *Pim1*^{+/-} mice. (L) Real-time PCR analysis of mRNA levels of Wnt signaling pathway-related genes in IECs from WT and *Pim1*^{+/-} mice ($n = 8$ from 2 independent experiments). The data represent the mean \pm SD. Statistical significance was determined by unpaired Student's *t*-test (H, J, and L).

UC patients from the publicly available GEO database (Spearman's rank correlation coefficient, $r = -0.318$, statistical analysis is performed using linear regression, $P = 0.0058$). (M) Representative confocal images and quantification of MUC2 staining (red) and DAPI (blue) in the indicated Caco2 cells ($n = 3$ from 3 independent experiments). Scale bar: $10 \mu\text{m}$. The data represent the mean \pm SD. Statistical significance was determined by unpaired Student's *t*-test (I–K) or one-way ANOVA (M).

colorectal cancer and PIM1 has been implicated in the tumorigenesis³⁷, we sought to examine whether epithelial PIM1 overexpression promotes AOM/DSS-induced colitis-associated colon cancer. We found that *Pim1*^{K1}Villin-Cre mice exhibited more

significant weight loss, increased tumor burden in the colon, and more severe colorectal tissue damage (Fig. 7A–D). Moreover, IHC analysis revealed that epithelial PIM1 overexpression led to a significant increase in colorectal tumor proliferation, as indicated

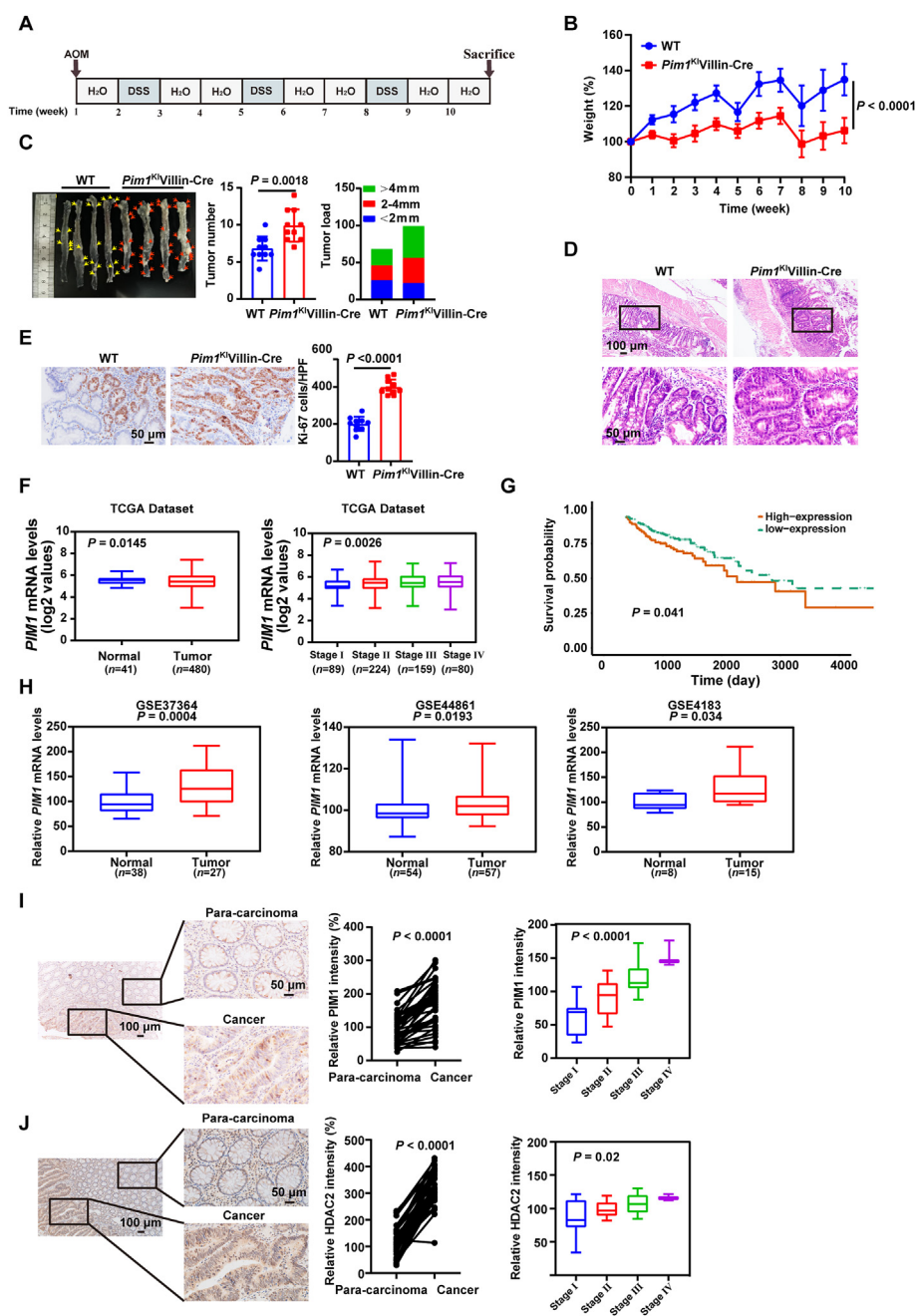


Figure 7 Epithelial PIM1 overexpression promotes AOM/DSS-induced CAC. (A–E) WT and *Pim1*^{K1}Villin-Cre mice were treated with AOM/DSS ($n = 10$ from 2 independent experiments). (A) Schematic overview of the AOM/DSS-induced CAC model. (B) Body weight loss of AOM/DSS-treated WT and *Pim1*^{K1}Villin-Cre mice. (C) Quantitation of tumor number and load in colonic tissues from WT and *Pim1*^{K1}Villin-Cre mice. (D) Representative images of H&E staining in colonic tumor tissues from WT and *Pim1*^{K1}Villin-Cre mice. (E) Immunohistochemistry staining and quantitation of Ki-67 in colonic tumor tissues from WT and *Pim1*^{K1}Villin-Cre mice. (F) *PIM1* mRNA expression levels in the CRC cohort from TCGA (left). *PIM1* mRNA expression levels at different tumor stages (right). (G) Kaplan–Meier analysis of the overall survival of the CRC cohort from TCGA. (H) Box plot of *PIM1* mRNA expression in normal tissues and CRC tissues from the GEO database. (I, J) Immunohistochemistry staining and quantitation of PIM1 (I) and HDAC2 (J) in para-carcinoma and cancer tissues (left) ($n = 44$). PIM1 and HDAC2 expression levels at different tumor stages from I to IV (right). Scale bar: 50 μ m or 100 μ m. The data represent the mean \pm SD. Statistical significance was determined by two-way ANOVA (B), unpaired Student's *t*-test (C, E, F, and H), one-way ANOVA (F, I, and J), or paired Student's *t*-test (I, J).

by higher proportions of Ki-67 positive cells in *Pim1*^{K1}Villin-Cre mice (Fig. 7E). These results suggest that *Pim1*^{K1}Villin-Cre mice are highly susceptible to CAC. Conversely, *Pim1*^{+/-} mice were more resistant to AOM/DSS-induced CAC than WT mice, as evidenced by less weight loss, lower tumor burden, and slower tumor proliferation rate than WT mice (Fig. S8A–S8D).

To further elucidate the effect of PIM1 on tumorigenesis, we analyzed PIM1 in the CRC cohort from The Cancer Genome Atlas (TCGA). *PIMI* was markedly increased in tumor tissues compared to normal tissues, and significantly higher *PIMI* expression was found for patients with advanced stage of CRC (Fig. 7F). Kaplan–Meier analysis revealed that PIM1 expression was negatively associated with the survival of CRC patients (Fig. 7G). Besides, analyses of public datasets further validated the higher expression of *PIMI* in CRC tissues compared with healthy controls (datasets from NCBI's Gene Expression Omnibus: GSE37364, GSE44861, and GSE4183) (Fig. 7H). Moreover, in clinical specimens, PIM1 and HDAC2 protein levels were upregulated in CRC tissues compared with matched para-carcinoma tissues (Fig. 7I and J). PIM1 and HDAC2 expression increased with advancing TNM (the most widely used cancer staging system) stage of CRC (Fig. 7I and J). Meanwhile, the results were confirmed in the CRC tissue chip using IHC (Fig. S8E and S8F). Together, these results suggest the significance of epithelial PIM1 overexpression in the progression of CAC tumorigenesis.

4. Discussion

Previous studies show that PIM1 inhibitors have protective effects against colitis, accompanied by inhibiting proinflammatory immune responses^{21,22}. However, the molecular mechanisms of PIM1 kinase in ulcerative colitis remain unknown. In the current study, we demonstrated the critical role of PIM1 in colonic goblet cell differentiation, which affects intestinal homeostasis.

Goblet cells are critical for the maintenance of the colonic barrier through the production of mucus³⁸. Goblet cells are derived from crypt-residing intestinal stem cells³⁹. Differentiation from stem cells to goblet cells involves a variety of complex signaling pathways, such as Wnt, Notch, PI3-kinase/Akt, and bone morphogenetic protein (BMP) signaling. Our findings indicate that PIM1 deficiency negatively regulates Wnt and Notch signaling in colonic epithelial cells. Additionally, we observed inhibition of the FoxO and MAPK signaling pathways in IECs from *Pim1*^{+/-} mice. FoxO signaling pathway is believed to play essential roles in the cell cycle, cell death, mitochondrial metabolism, oxidative stress response, and autophagy. Recently, it was shown that FoxO signaling pathway inhibition decreases the expression of stem cell markers and impairs stem cell renewal⁴⁰. Another study showed FoxO and Notch signaling converge on regulating mitochondrial fission that promotes stem cell differentiation into goblet cells and Paneth cells⁴¹. MAPK signaling pathways regulate intestinal epithelial cell growth and Paneth cell differentiation. Recent studies have revealed that inhibition of MAPK signaling pathways promotes Paneth cell differentiation and expands the ISC population by activating the Wnt signaling pathway^{42,43}. Another study showed that activation of MAPK signaling pathways promotes goblet cell differentiation in a Notch signaling pathway-dependent manner⁴⁴. These studies suggest that the role of FoxO and MAPK signaling pathways in intestinal homeostasis is complicated. Overall, the maintenance and differentiation of intestinal stem cells are tightly regulated by several critical signaling pathways.

Wnt and Notch signaling pathways are the main signaling pathways that regulate intestinal stem cell proliferation and differentiation.

HDAC2 plays an essential role in the epigenetic regulation of gene expression by removing the acetyl groups on a histone of the specific gene⁴⁵. Here, we showed that PIM1 modulated HDAC2 protein levels and that HDAC2 acted as a negative regulator of the Wnt signaling pathway by binding with the promoter to enhance goblet cell differentiation. Moreover, previous studies suggest that IEC-specific HDAC1/2 deletion represses secretory cell development and modulates the activation of Notch signaling^{28,46}. However, the effect of PIM1-mediated HDAC2 modulation on Notch signaling was not apparent in our study. Together, HDAC2-dependent epigenetic modification provides novel insight into the molecular mechanisms underlying PIM1-regulated goblet cell differentiation.

Overwhelming evidence suggests that various post-translational modifications, such as phosphorylation, acetylation, ubiquitination, SUMOylation, nitrosylation, and carbonylation, regulate HDAC2 expression. Among the various post-translational modifications, HDAC2 phosphorylation has been well studied²⁴. It has been demonstrated that HDAC2 phosphorylation by CK2 promotes its ubiquitination and subsequent degradation in human bronchial epithelial and primary small airway epithelial cells⁴⁷. However, phosphorylation of HDAC2 at Y222 by c-Abl tyrosine kinase increases its stability and prevents HDAC2 proteasomal degradation⁴⁸. Thus, there is a discrepancy in the effect of HDAC2 phosphorylation on its protein level. We discovered that HDAC2 phosphorylation by PIM1 decreased its level *in vitro*. Accordingly, PIM1 reduced HDAC2 expression under both basal and DSS-induced colitis conditions. Whether HDAC2 phosphorylation by PIM1 impacts its transcriptional repression activity awaits further investigations.

Studies have demonstrated that PIM1 promotes the occurrence and development processes of tumors through phosphorylating various proteins and is highly expressed in several cancers, especially CRC⁴⁹. Colitis-associated colorectal cancer (CAC), a subtype of CRC closely associated with ulcerative colitis, is more dangerous than sporadic CRC⁵⁰. Although the role of PIM1 in CRC has been demonstrated, the function of PIM1 in CAC remains unclear. In this study, we identified that overexpression of PIM1 in IECs promoted the development of CAC, suggesting that PIM1 may be a potential target for the treatment of CAC.

5. Conclusions

Our study defines previously unknown functions of PIM1 as a critical regulator of goblet cell differentiation, providing a better understanding of PIM1 in intestinal homeostasis. Increased expression of PIM1 kinase has been observed in colonic tissues from UC patients, suggesting its potential as a biomarker and therapeutic target for UC.

Acknowledgments

We thank Professor Zebin Mao and Wenhua Yu (Peking University Health Science Center), and Professor Kai Zhang (Tianjin Medical University) for providing help with mice and LC–MS/MS experiments. This study was supported by grants from the National Natural Science Foundation of China (NSFC) Programs (32170186, 82200618, 82173199), Tianjin Science and

Technology Commissioner Project (22JCZDJC00490, 22JCQNJC00540, China).

Author contributions

Quan Wang and Zhi Yao designed and supervised the study. Jianming Yang, Yawen Xiao, Ningning Zhao, and Xinyu Sun performed the majority of experiments. Geng Pei, Yan Sun, Hongyu Chu, Lu Zhou, and Bangmao Wang prepared the Human samples, and Kaiyuan Yu, Chunhui Miao, Ran Liu, and Junqiang Lv provided help with experimental technology. Quan Wang, Jianming Yang, and Zhi Yao analyzed the data and wrote the paper. All authors discussed the data and reviewed the manuscript.

Conflicts of interest

The authors declare no competing interests.

Appendix A. Supporting information

Supporting information to this article can be found online at <https://doi.org/10.1016/j.apsb.2024.04.017>.

References

- Kobayashi T, Siegmund B, Le Berre C, Wei SC, Ferrante M, Shen B, et al. Ulcerative colitis. *Nat Rev Dis Prim* 2020;**6**:74.
- Burisch J, Zhao M, Odes S, De Cruz P, Vermeire S, Bernstein CN, et al. The cost of inflammatory bowel disease in high-income settings: a Lancet Gastroenterology & Hepatology Commission. *Lancet Gastroenterol Hepatol* 2023;**8**:458–92.
- Du L, Ha C. Epidemiology and pathogenesis of ulcerative colitis. *Gastroenterol Clin N Am* 2020;**49**:643–54.
- An J, Liu Y, Wang Y, Fan R, Hu X, Zhang F, et al. The role of intestinal mucosal barrier in autoimmune disease: a potential target. *Front Immunol* 2022;**13**:871713.
- Gelmez E, Jeron A, Bruder D. Negative elongation factor: a key factor in the maintenance of intestinal epithelial barrier integrity. *Cell Mol Immunol* 2022;**19**:453–5.
- Okumura R, Takeda K. Maintenance of intestinal homeostasis by mucosal barriers. *Inflamm Regen* 2018;**38**:5.
- Gustafsson JK, Johansson MEV. The role of goblet cells and mucus in intestinal homeostasis. *Nat Rev Gastroenterol Hepatol* 2022;**19**:785–803.
- Kang Y, Park H, Choe BH, Kang B. The role and function of mucins and its relationship to inflammatory bowel disease. *Front Med* 2022;**9**:848344.
- van der Post S, Jabbar KS, Birchenough G, Arike L, Akhtar N, Sjøvall H, et al. Structural weakening of the colonic mucus barrier is an early event in ulcerative colitis pathogenesis. *Gut* 2019;**68**:2142–51.
- Heazlewood CK, Cook MC, Eri R, Price GR, Tauro SB, Taupin D, et al. Aberrant mucin assembly in mice causes endoplasmic reticulum stress and spontaneous inflammation resembling ulcerative colitis. *PLoS Med* 2008;**5**:e54.
- Wenzel UA, Magnusson MK, Rydstrom A, Jonstrand C, Hengst J, Johansson ME, et al. Spontaneous colitis in Muc2-deficient mice reflects clinical and cellular features of active ulcerative colitis. *PLoS One* 2014;**9**:e100217.
- Gundamaraju R, Chong WC. Consequence of distinctive expression of MUC2 in colorectal cancers: how much is actually bad? *Biochim Biophys Acta Rev Cancer* 2021;**1876**:188579.
- McCauley HA, Guasch G. Three cheers for the goblet cell: maintaining homeostasis in mucosal epithelia. *Trends Mol Med* 2015;**21**:492–503.
- Narlik-Grassow M, Blanco-Aparicio C, Carnero A. The PIM family of serine/threonine kinases in cancer. *Med Res Rev* 2014;**34**:136–59.
- Panchal NK, Sabina EP. A serine/threonine protein PIM kinase as a biomarker of cancer and a target for anti-tumor therapy. *Life Sci* 2020;**255**:117866.
- Qian KC, Wang L, Hickey ER, Studts J, Barringer K, Peng C, et al. Structural basis of constitutive activity and a unique nucleotide binding mode of human Pim-1 kinase. *J Biol Chem* 2005;**280**:6130–7.
- Bellon M, Nicot C. Targeting Pim kinases in hematological cancers: molecular and clinical review. *Mol Cancer* 2023;**22**:18.
- Braso-Maristany F, Filosto S, Catchpole S, Marlow R, Quist J, Francesch-Domenech E, et al. PIM1 kinase regulates cell death, tumor growth and chemotherapy response in triple-negative breast cancer. *Nat Med* 2016;**22**:1303–13.
- Li H, Xie L, Zhu L, Li Z, Wang R, Liu X, et al. Multicellular immune dynamics implicate PIM1 as a potential therapeutic target for uveitis. *Nat Commun* 2022;**13**:5866.
- Wang X, Cheng W, Chen X, Gong Y, Wang G, Zhang X, et al. Inhibition of CEBPB attenuates lupus nephritis via regulating Pim-1 signaling. *Mediat Inflamm* 2022;**2022**:2298865.
- Shen Y, Xie Y, Zhao Y, Long Y, Li L, Zeng Y. Pim-1 inhibitor attenuates trinitrobenzene sulphonic acid induced colitis in mice. *Clin Res Hepatol Gastroenterol* 2018;**42**:382–6.
- Shen YM, Zhao Y, Zeng Y, Yan L, Chen BL, Leng AM, et al. Inhibition of Pim-1 kinase ameliorates dextran sodium sulfate-induced colitis in mice. *Dig Dis Sci* 2012;**57**:1822–31.
- Jo H, Shim K, Kim HU, Jung HS, Jeoung D. HDAC2 as a target for developing anti-cancer drugs. *Comput Struct Biotechnol J* 2023;**21**:2048–57.
- Bahl S, Seto E. Regulation of histone deacetylase activities and functions by phosphorylation and its physiological relevance. *Cell Mol Life Sci* 2021;**78**:427–45.
- Gediya P, Parikh PK, Vyas VK, Ghate MD. Histone deacetylase 2: a potential therapeutic target for cancer and neurodegenerative disorders. *Eur J Med Chem* 2021;**216**:113332.
- Liang T, Wang F, Elhassan RM, Cheng Y, Tang X, Chen W, et al. Targeting histone deacetylases for cancer therapy: trends and challenges. *Acta Pharm Sin B* 2023;**13**:2425–63.
- Sun X, Shu Y, Ye G, Wu C, Xu M, Gao R, et al. Histone deacetylase inhibitors inhibit cervical cancer growth through Parkin acetylation-mediated mitophagy. *Acta Pharm Sin B* 2022;**12**:838–52.
- Gonneaud A, Turgeon N, Boudreau F, Perreault N, Rivard N, Asselin C. Distinct roles for intestinal epithelial cell-specific Hdac1 and Hdac2 in the regulation of murine intestinal homeostasis. *J Cell Physiol* 2016;**231**:436–48.
- Sann H, Erichsen J, Hessmann M, Pahl A, Hoffmeyer A. Efficacy of drugs used in the treatment of IBD and combinations thereof in acute DSS-induced colitis in mice. *Life Sci* 2013;**92**:708–18.
- Guo Y, Zhang Z, Wei H, Wang J, Lv J, Zhang K, et al. Cytotoxic necrotizing factor 1 promotes prostate cancer progression through activating the Cdc42–PAK1 axis. *J Pathol* 2017;**243**:208–19.
- Smillie CS, Biton M, Ordovas-Montanes J, Sullivan KM, Burgin G, Graham DB, et al. Intra- and inter-cellular rewiring of the human colon during ulcerative colitis. *Cell* 2019;**178**:714–30.
- Liu Y, Shang Y, Yan Z, Li H, Wang Z, Liu Z, et al. Pim1 kinase positively regulates myoblast behaviors and skeletal muscle regeneration. *Cell Death Dis* 2019;**10**:773.
- Yao D, Dai W, Dong M, Dai C, Wu S. MUC2 and related bacterial factors: therapeutic targets for ulcerative colitis. *EBioMedicine* 2021;**74**:103751.
- Vancamelbeke M, Vermeire S. The intestinal barrier: a fundamental role in health and disease. *Expert Rev Gastroenterol Hepatol* 2017;**11**:821–34.
- Zhang X, Han Y, Huang W, Jin M, Gao Z. The influence of the gut microbiota on the bioavailability of oral drugs. *Acta Pharm Sin B* 2021;**11**:1789–812.
- Asati V, Mahapatra DK, Bharti SK. PIM kinase inhibitors: structural and pharmacological perspectives. *Eur J Med Chem* 2019;**172**:95–108.

37. Shah SC, Itzkowitz SH. Colorectal cancer in inflammatory bowel disease: mechanisms and management. *Gastroenterology* 2022;**162**: 715–30.
38. Nystrom EEL, Martinez-Abad B, Arike L, Birchenough GMH, Nonnecke EB, Castillo PA, et al. An intercrypt subpopulation of goblet cells is essential for colonic mucus barrier function. *Science* 2021;**372**:eabb1590.
39. Johansson ME, Hansson GC. Goblet cells need some stress. *J Clin Invest* 2022;**132**:e162030.
40. Ludikhuize MC, Rodriguez Colman MJ. Metabolic regulation of stem cells and differentiation: a forkhead box O transcription factor perspective. *Antioxidants Redox Signal* 2021;**34**:1004–24.
41. Ludikhuize MC, Meerlo M, Gallego MP, Xanthakis D, Burgaya Julia M, Nguyen NTB, et al. Mitochondria define intestinal stem cell differentiation downstream of a FOXO/Notch axis. *Cell Metabol* 2020;**32**:889–900.
42. Wei G, Gao N, Chen J, Fan L, Zeng Z, Gao G, et al. Erk and MAPK signaling is essential for intestinal development through Wnt pathway modulation. *Development* 2020;**147**:dev185678.
43. Grinat J, Kosel F, Goveas N, Kranz A, Alexopoulou D, Rajewsky K, et al. Epigenetic modifier balances Mapk and Wnt signalling in differentiation of goblet and Paneth cells. *Life Sci Alliance* 2022;**5**: e202101187.
44. Feng Y, Bommer GT, Zhao J, Green M, Sands E, Zhai Y, et al. Mutant KRAS promotes hyperplasia and alters differentiation in the colon epithelium but does not expand the presumptive stem cell pool. *Gastroenterology* 2011;**141**:1003–13.
45. Wang Z, Zang C, Cui K, Schones DE, Barski A, Peng W, et al. Genome-wide mapping of HATs and HDACs reveals distinct functions in active and inactive genes. *Cell* 2009;**138**:1019–31.
46. Gonneaud A, Turgeon N, Boisvert FM, Boudreau F, Asselin C. JAK–STAT pathway inhibition partially restores intestinal homeostasis in *Hdac1*- and *Hdac2*-intestinal epithelial cell-deficient mice. *Cells* 2021;**10**:224.
47. Adenuga D, Rahman I. Protein kinase CK2-mediated phosphorylation of HDAC2 regulates co-repressor formation, deacetylase activity and acetylation of HDAC2 by cigarette smoke and aldehydes. *Arch Biochem Biophys* 2010;**498**:62–73.
48. Gonzalez-Zuniga M, Contreras PS, Estrada LD, Chamorro D, Villagra A, Zanlungo S, et al. c-Abl stabilizes HDAC2 levels by tyrosine phosphorylation repressing neuronal gene expression in Alzheimer's disease. *Mol Cell* 2014;**56**:163–73.
49. Toth RK, Warfel NA. Targeting PIM kinases to overcome therapeutic resistance in cancer. *Mol Cancer Therapeut* 2021;**20**:3–10.
50. Nagao-Kitamoto H, Kitamoto S, Kamada N. Inflammatory bowel disease and carcinogenesis. *Cancer Metastasis Rev* 2022;**41**:301–16.